Positive muons as probes in ferromagnetic metals

Autor(en): **Denison, A.B. / Graf, H. / Kündig, W.**

Objekttyp: **Article**

Zeitschrift: **Helvetica Physica Acta**

Band (Jahr): **52 (1979)**

Heft 4

PDF erstellt am: **21.09.2024**

Persistenter Link: https://doi.org/10.5169/seals-115037

Helvetica Physica Acta, Vol. 52 (1979), Birkhäuser Verlag, Basel

Positive muons as probes in ferromagnetic metals*

A. B. Denison[a]), **H. Graf**[b]), **W. Kündig** and **P. F. Meier**

Physik-Institut der Universität Zürich, Zürich, Switzerland

(17. VII. 1979)

Abstract. A comprehensive account of μSR (muon spin rotation) experiments in ferromagnetic metals performed at SIN is given. The μSR technique is described, and the contributions to the local magnetic field at a positive muon in magnetic metals are discussed. Measurements in Co, Gd, Dy, Fe, and Ni are reported and the observed frequencies and relaxation rates as a function of temperature and external applied field are analyzed. In particular, the determination of the stopping site of the muon and the resulting hyperfine field values are discussed.

I. Introduction

The advent of the new generation of high intensity intermediate energy accelerators, the so-called meson factories, allows solid state physicists to use the muon as a microscopic probe to study magnetic and electronic properties of matter.

If spin polarized muons are stopped in a solid, the muon spin will precess with the Larmor frequency in the local magnetic field. An important feature of the muon used in solid state experiments is its parity-violating decay with a mean lifetime of 2.2 μs into a positron and two neutrinos with the positron emitted preferentially along the muon spin direction. By detecting the time-dependent angular correlation pattern of the decay positron, the precession of the muon spin can be observed. Thus the muon spin rotation (μSR) technique measures the local field directly. The first μSR experiment was performed in 1957 by Garwin, Lederman, and Weinrich [1]. In this famous experiment the parity-violation in both the $\pi \rightarrow \mu + \nu_\mu$ and the $\mu \rightarrow e + \nu_\mu + \nu_e$ decays was shown. Applications to solid state physics were scarce until about 1970, but since that time the μSR has developed into a powerful tool in solid state physics. Although the method is limited by the few existing meson factories the number of experiments reported has increased markedly. The general status of μSR research today is summarized in a review article by Brewer and Crowe [2], and more recently in the Proceedings of the First International Topical Meeting on Muon Spin Rotation [3] held in 1978 in Rorschach, (Switzerland).

In the present work a comprehensive survey is made of systematic μSR studies on a set of ferromagnetic metals performed at the Swiss Institute for

* Work supported in part by the Swiss National Science Foundation.

[a]) on sabbatical leave from University of Wyoming.

[b]) present address: University of Konstanz, Germany.

Nuclear Research (SIN). After an introduction to the μSR technique and a description of our apparatus, experiments on the ferromagnetic transition metals Fe, Co, Ni and the ferromagnetic rare earth metals Gd and Dy are described. The fundamental contributions to the measured local fields are investigated and considered in terms of each substance studied. In particular, the experiments have demonstrated the importance of the magnetic dipolar fields. The results give useful information on the interstitial magnetization (spin density). In some cases it was possible to uniquely determine the interstitial muon stopping site. From the measured relaxation behaviour, one may learn about muon diffusion and the influence of defects. This is of importance to the related problem of hydrogen diffusion in metals, since the muon in many ways behaves as a light proton. In the concluding section the results of the various ferromagnetic metals are compared and a discussion is given concerning the questions yet to be answered in the understanding of the muon's interaction with its host.

II. The μSR-technique

To the best of present-day knowledge the muon is nothing but a heavy electron. Some of its properties are [4]:

mass	$m_\mu = 105.6595\ \text{MeV}/c^2 = 206.7687\ m_e = 0.1126098\ m_p$
spin	$I_\mu = \frac{1}{2}$
lifetime	$\tau_\mu = 2.19713\ \mu\text{s}$
magnetic moment	$\mu_\mu = 4.49047 \times 10^{-26}\ \text{J/T} = 3.183340\ \mu_p$
g-factor	$g_\mu = 2 \times 1.0011662$
gyromagnetic ratio	$\gamma_\mu/2\pi = 135.5374\ \text{MHz/T} = 13.55374\ \text{MHz/kG}.$

The main decay modes of the negative muon and its positive antiparticle are:

$$\mu^- \rightarrow e^- + \nu_\mu + \bar{\nu}_e,$$
$$\mu^+ \rightarrow e^+ + \bar{\nu}_\mu + \nu_e.$$

The negative muon will be captured by the atoms in a solid. The X-rays emitted in cascading down through the various shells give mainly information on atomic and nuclear properties. Since the negative muon loses a large fraction of its polarization during the cascade, its value to investigate local fields related with solid state properties is limited. The positive muon, repelled by the positive ion cores will probe preferentially interstitial lattice sites. In the following discussion only the positive muon will be considered.

Under the assumption of the two-component neutrino theory, where only V and A interactions are present, the β-spectrum of the muon decay is described in detail in Ref. 5. To a good approximation (neglecting the electron rest mass compared to its momentum, $p_e \cong mc$, and small QED corrections), one may write for the angular correlation of the parity violating muon decay

$$dW(\theta, \varepsilon, t) = \frac{\varepsilon^2}{\pi\tau_\mu}(3-2\varepsilon)\left[1-\frac{1-2\varepsilon}{3-2\varepsilon}\cos\theta\right]\exp(-t/\tau_\mu)\, d\Omega\, d\varepsilon\, dt, \qquad (1)$$

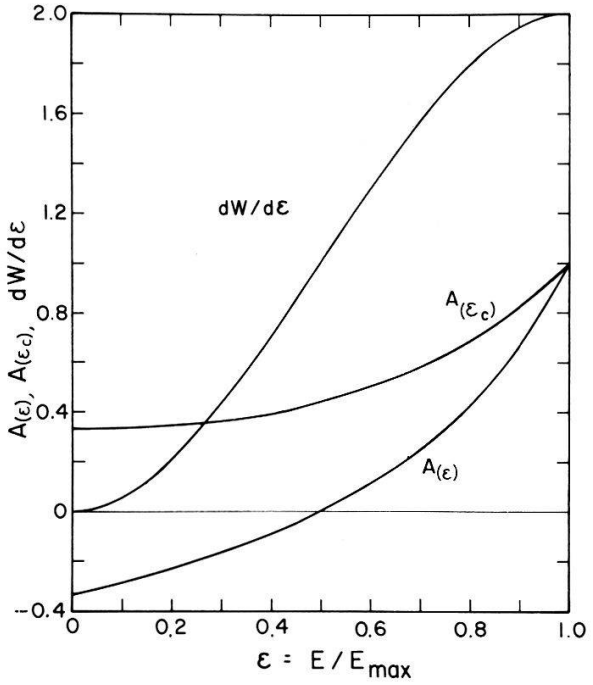

Figure 1
β-spectrum of the positrons emitted in the muon decay ($dW/d\varepsilon$). $A(\varepsilon)$ is the energy-dependent asymmetry. $A(\varepsilon_c)$ is the asymmetry if all the positrons above the cut-off energy ε_c are detected.

where θ is the angle between the positron momentum and the muon spin. ε is the positron energy in units of its maximum possible energy ($\varepsilon = E/E_{\max}$). The maximum kinetic energy is

$$E_{\max} = \frac{m_\mu c^2}{2} - m_e c^2 \left(1 - \frac{m_e}{m_\mu}\right) = 52.320\ \text{MeV}. \tag{2}$$

The only change of the above angular correlation formula (1) in the case of the μ^--decay is a change in the sign of the cosine term.

The energy spectrum obtained by integration of equation (1) is given by:

$$dW(\varepsilon) = (6\varepsilon^2 - 4\varepsilon^3)\, d\varepsilon \tag{3}$$

and is plotted in Fig. 1. The asymmetry

$$A(\varepsilon) = -(1-2\varepsilon)/(3-2\varepsilon) \tag{4}$$

is strongly energy-dependent as is also shown in Fig. 1. At $\varepsilon = 1$ ($E = E_{\max}$) the asymmetry A is equal to one indicating that 'all' the positrons are emitted in the muon spin direction. This follows from the simple argument that at $E = E_{\max}$ the two neutrinos are emitted exactly in the opposite direction to the positron. Due to angular momentum conservation and the positive helicity of the positron it is easily shown that the positron is emitted in the muon spin direction. For energies below $\varepsilon = \frac{1}{2}$ the positrons are preferentially emitted in the muon spin backward direction ($A < 0$). If all the positrons are detected one gets by the integration of equation (1) over ε

$$dW(\theta) = \frac{1}{4\pi}(1 + \tfrac{1}{3}\cos\theta)\, d\Omega. \tag{5}$$

By appropriate absorbers between the target and the positron detectors it is possible to eliminate the low energy positrons. This will increase the measured asymmetry, but decrease the counting rate. The asymmetry $A(\varepsilon_c)$ plotted as a function of the low energy positron cut-off ε_c is shown in Fig. 1.

To efficiently use the valuable beam time it is important to optimize the statistical accuracy of the measurements by eliminating the low energy positrons by appropriate absorbers. This statistical problem will be treated in Appendix A.

The polarized muons are produced by the pion decay

$$\pi^+ \rightarrow \mu^+ + \nu_\pi \, (\tau_\pi = 26.03 \text{ ns}, \, m_\pi = 139.569 \text{ MeV}/c^2).$$

The pion lifetime corresponds to a mean free path at $p_\pi = 200$ MeV/c ($v = 0.82\,c$) of 6.4 m. In the pion rest system the muons have a momentum of 29.790 MeV/c corresponding to a kinetic energy of 4.1192 MeV. It is seen that in the pion rest-system the muons are 100% longitudinally polarized (see Fig. 2). The neutrino ν_μ has a negative helicity. Momentum and angular momentum conservation require that the muon is 100% backward polarized.

The experiments described here were performed in the muon beam at the Swiss Institute for Nuclear Research (SIN). The pions produced by the 590 MeV

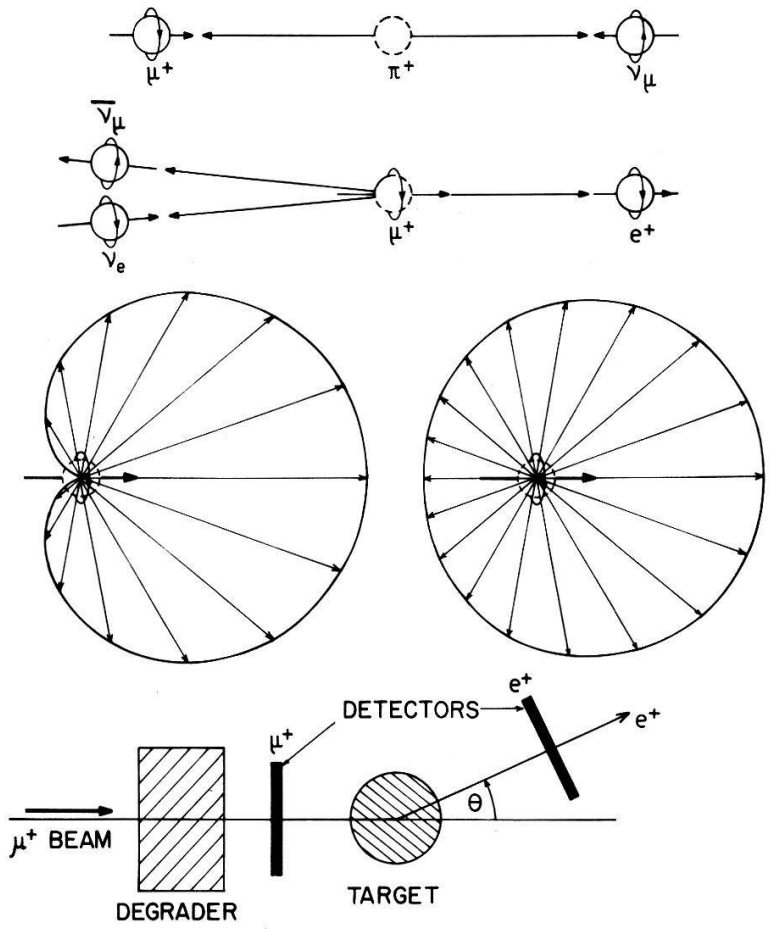

Figure 2
The upper part of the figure illustrates the π^+ and μ^+ decay. In the center the angular distribution patterns of the decay positrons with respect to the μ^+ spin are shown for the case that only positrons at the maximum energy are registered (left) and for the case that all the positrons are detected (right). In the lower part a simplified diagram of the counter and target arrangement is shown.

proton beam decay in flight in the so-called muon channel, an 8 m long 12 cm diameter 50 kG superconducting solenoid. The muons accepted by the solenoid are emitted in the pion rest frame under an angle ϕ of approximately 0 or π with respect to the pion momentum. The muons emitted in the forward direction ($\phi = 0$) are backward polarized and vice versa. The momenta of the for- and backward polarized muons in the laboratory frame of reference are:

$$p_\mu c = p_\pi c \frac{m_\pi^2 + m_\mu^2}{2m_\pi^2} \mp \frac{m_\pi^2 - m_\mu^2}{2m_\pi^2} (m_\pi^2 c^4 + p_\pi^2 c^2)^{1/2}. \tag{6}$$

For a typical pion momentum of $p_\pi = 200\,\mathrm{MeV}/c$ one gets for the resulting backward polarized muon a momentum of 209.37 MeV/c, for the forward polarized muons a momentum of 105.26 MeV/c. In the experiment described, the forward polarized muons are used. This is partially due to the smaller stopping range and the reduced straggling of the muons in the target. Due to kinematic depolarization and the finite angular resolution the experimentally determined muon polarization is reduced to roughly 80%.

In a typical μSR experiment the polarized positive muons are stopped in the material to be investigated (Fig. 2), and the time dependent angular correlation pattern $W(\theta, t)$ is measured. A clock (e.g. a time to amplitude converter) is started as the muon enters the target and stopped when the decay positron is detected in a second scintillator array. In the short time of thermalization ($\sim 10^{-13}$ s) the muon maintains its polarization. If a magnetic field B is applied perpendicular to the initial muon polarization the muon spin precesses with the Larmor frequency $\omega/2\pi = g_\mu Be/(4\pi m_\mu) = \gamma_\mu B/2\pi$ and one may write for the experimental time dependent counting rate

$$N(\theta, t) = N_0\{\exp(-t/\tau_\mu)[1 + A_{\mathrm{eff}} P(t) \cos(\theta + \omega t)] + b\}, \tag{7}$$

where b is the background, N_0 a normalization constant and A_{eff} an effective anisotropy. $P(t)$ is a transverse relaxation function. In the examples discussed here the relaxation function may be written in the simplified form $P(t) = \exp(-t/T_2)$, where T_2 is the transverse relaxation time known from magnetic resonance.

The effective anisotropy constant, A_{eff}, takes into account the reduction of the anisotropy due to geometrical effects and unmeasured fast depolarization effects. For these sample dependent fast depolarization effects (time scale $\lesssim 10^{-9}$ s) a satisfactory explanation has not been found. Impurities, crystal defects, field inhomogeneities, and muonium formation in the initial stage may be responsible for the fast depolarization.

Figure 3 shows an example of a μSR spectrum measured in polycrystalline copper in an external field of 506 G. The measured points were fitted to equation (7). Superimposed on the exponential muon decay one observes an oscillation in the positron counting rate due to the Larmor precession.

In the following some of the technical details of the μSR facility will be described (see Fig. 4).

The forward polarized muons are slowed down in the degrader so that most of them are stopped in the target to be investigated. As degrader material, polyethylene and a variable amount of water in a cylindrical piston arrangement are used. The water degrader can be set externally for maximum μ stop rate in the target.

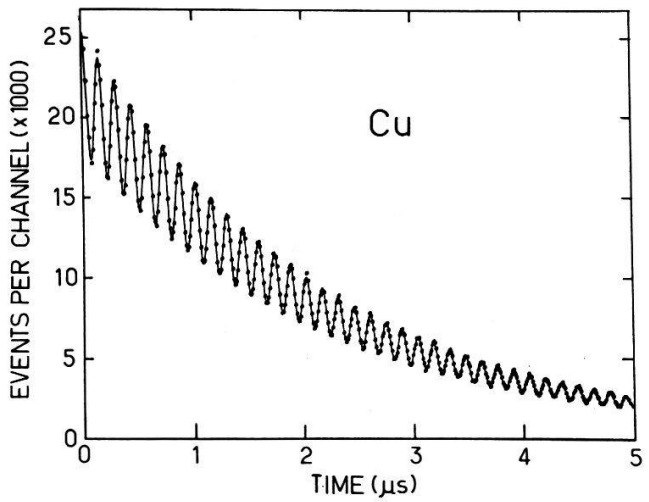

Figure 3
μSR spectrum of Cu in transverse magnetic field of 506 G. The oscillations superimposed on the exponential muon decay are due to the muon spin precession. The line plotted corresponds to the least square fit to equation (7).

As detectors, plastic scintillators NE 102 and NE 111 mounted via light pipes on XP 2020 and AVP 56 multipliers are used. The light pipes (about 120 cm) and various magnetic shielding tubes were used to reduce the influence of the magnetic field on the multipliers.

The magnetic field is generated by a pair of Helmholtz coils with a rating of 6 kG at 70 kW. The field homogeneity was checked with a Hall probe and found to be better than 10^{-4} in a volume of $12\times12\times12$ mm^3. The long term stability of the power supply was specified (at 6 kG) to be 1×10^{-4}. The ripple specified as 5×10^{-4} could be reduced with correction coils. A pick-up coil together with a feedback circuit was used to generate the ripple compensation current. For fields

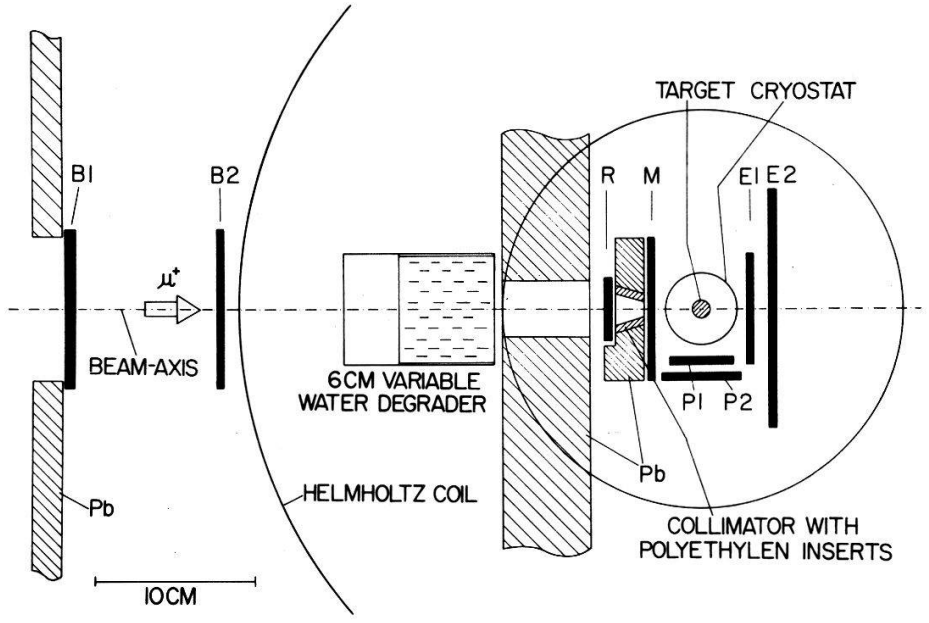

Figure 4
Schematic diagram of the μSR apparatus. The field produced by the Helmholtz coils is perpendicular to the figure.

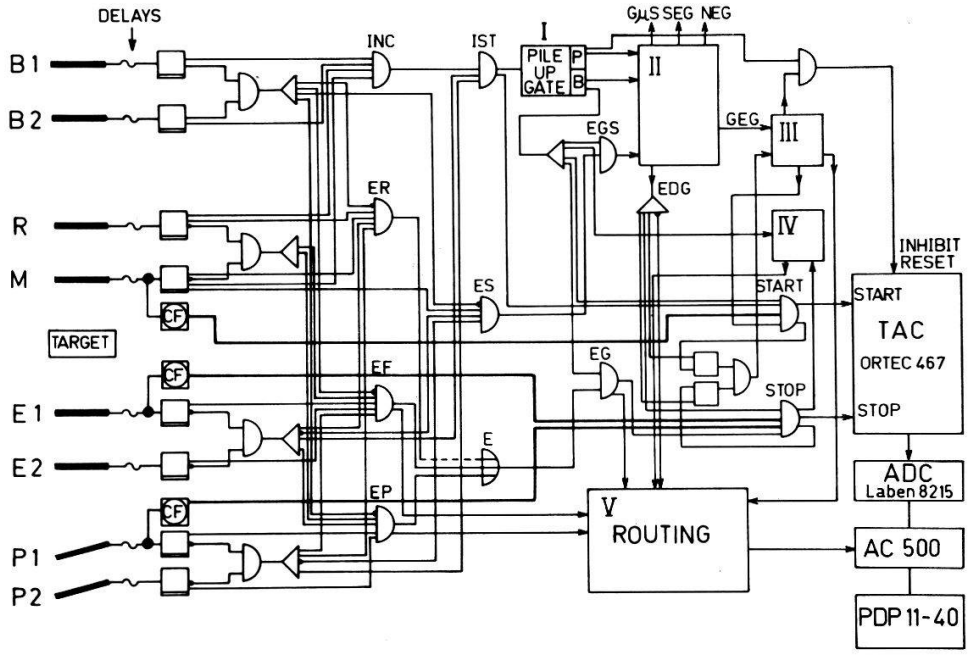

Figure 5
Block diagram of the μSR electronics. B1, B2, R, and M are muon counters, E1 and E2 the forward positron counters, and P_1 and P_2 the perpendicular positron counters.

below 200 G a small current stabilized power supply was used. The current and thus the field is monitored with a digital voltmeter measuring the voltage drop over a 500 A shunt. The field was calibrated with an NMR probe above 1 kG. Stray fields and the earth field are compensated by the use of 6 square coils of the dimension $1 \times 1\ m^2$ mounted on the sides of a $1\ m^3$ cube. The present Hall probe arrangement allows a zero field setting within ±5 mG.

Figure 5 shows a simplified schematic of the electronics. The detectors B_1, B_2, R and M register an incoming muon, the detectors E_1 and E_2 the positrons emitted in the forward direction, and P_1 and P_2 positrons emitted in the perpendicular direction ($\theta = 90°$). For the exact timing, *c*onstant *f*raction discriminators (CF) are used. As clock, a *t*ime to *a*mplitude *c*onverter (TAC) is used. By the routing unit the forward and perpendicular spectrum is routed to the corresponding memory section of a PDP computer. Great care is taken for the detected positrons to be properly correlated with the corresponding muons. Some of the coincidences formed are:

INC: $B_1 \cdot B_2 \cdot R \cdot M =$ *inc*oming muon

IST: $\text{INC} \cdot \bar{E}_1 \cdot \bar{E}_2 \cdot \bar{P}_1 \cdot \bar{P}_2 =$ *i*ncoming *st*opped muons

EF: $\bar{B}_1 \cdot \bar{B}_2 \cdot \bar{M} \cdot \bar{R} \cdot \bar{P}_1 \cdot \bar{P}_2 \cdot E_1 \cdot E_2 =$ *f*orward *e*lectron (positron)

EP: $\bar{B}_1 \cdot \bar{B}_2 \cdot \bar{M} \cdot \bar{R} \cdot \bar{E}_1 \cdot \bar{E}_2 \cdot P_1 \cdot P_2 =$ *p*erpendicular *e*lectron

ER: $\bar{B}_1 \cdot \bar{B}_2 \cdot R \cdot M \cdot \bar{E}_1 \cdot \bar{E}_2 \cdot \bar{P}_1 \cdot \bar{P}_2 =$ backward (*r*ückwärts) *e*lecton

The incoming muons (INC) produce in the pile-up gate a 6 μs busy signal which will reset the TAC if a second muon is detected during this time. The logic

is tested with pulsers simulating the muon and positron pulses. The time-scale is calibrated with a quartz-controlled 500 MHz TAC calibrator. Time zero is obtained by observing muons passing through the muon and positron detectors. These straight through pulses show a time resolution of 0.9 ns FWHM. This time resolution corresponds to an upper frequency limit of 550 MHz or a maximum magnetic field to observe the muon precession of ~40 kG. The frequency range can easily be checked by measuring the 'free' muonium in quartz [2]. The free muonium frequency corresponding to the Larmor precession of the Mu atom is esssentially given by the large magnetic moment of the electron, $\nu_{Mu} = \frac{1}{2}(\nu_{12}+\nu_{23}) = 1.394$ MHz B[G]. Control measurements show that Mu-frequencies up to 550 MHz can be detected. A program written in machine language allows on-line Fourier transformations and various controls during the measurements. Measurements can be done in various cryostats and ovens from 4 K to 1300 K.

III. The muon, a microscopic probe of magnetism

After thermalization by ionization processes the fate of the polarized muon depends critically on whether muonium ($\mu^+e^- = \mathrm{Mu}$) is formed or not.

In the hydrogenlike 'atom' muonium, the muon will precess in the hyperfine field produced by the electron at the muon site. The observed μSR precession frequencies measure directly the hyperfine interaction. In solids this gives information about the electronic environment. A good example is the existence of two muonium states observed in the semiconductor silicon [6]. In other materials the muonium may participate in chemical bonding. The muonium formation seems to be restricted to a few insulators and semiconductors.

In metals muonium has not been found. This is attributed to the screening of the muon charge by the conduction electrons. The bare muon will probe the local magnetic field B_μ at interstitial and in some cases at substitutional sites.

In ferro- and antiferromagnetic materials described here the local field may be written as

$$\vec{B}_\mu = \vec{B}_{ext} + \vec{B}_{dip} + \vec{B}_{hf}. \tag{8}$$

For ferromagnets the dipolar field is sometimes written as

$$\vec{B}_{dip} = \vec{B}_{dem} + \vec{B}_L + \vec{B}'_{dip}, \tag{9}$$

where $\vec{B}_{ext}$ is the external field, $\vec{B}_{dem} = -N\vec{M}$ is the shape dependent demagnetizing field (M = bulk magnetization density), $\vec{B}_L = (4\pi/3)\vec{M}_s$ is the Lorentz field in a domain (M_s = saturation magnetization density), $\vec{B}'_{dip}$ is the dipolar field from the dipoles within the Lorentz sphere, and $\vec{B}_{hf}$ is the hyperfine field (see Fig. 6). For an unmagnetized sample in zero external field B_{ext} and B_{dem} are zero. The hyperfine field (Fermi contact field) which is of interest for solid state physics is mainly due to the polarized conduction electron density at the muon site ($\vec{R}_\mu$).

$$B_{hf} = -\frac{8\pi}{3}\mu_B^e \rho_{spin}(\vec{R}_\mu) \tag{10}$$

is thus obtained from the measured field B_μ and the calculated field B'_{dip}. A prerequisite for such a calculation is the knowledge of the muon site. As will be

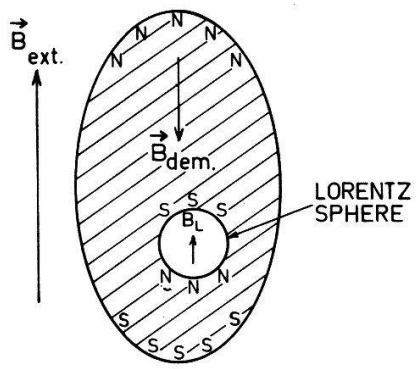

Figure 6
The field at a muon site in a ferromagnet may be written as $\vec{B}_\mu = \vec{B}_{ext} + \vec{B}_{dem} + \vec{B}_L + \vec{B}'_{dip} + \vec{B}_{hf}$. The origin of the first three terms is shown. $\vec{B}'_{dip}$ and $\vec{B}_{hf}$ are due to the atomic dipoles within the Lorentz-sphere and the polarized conduction electron at the muon site, respectively.

shown it was possible in several cases to determine the stopping site directly from μSR measurements.

Measurements in a magnetic material will give 3 quantities of interest

1) The field B_μ at the site of the muon
2) The relaxation time
3) The asymmetry A_{eff} extrapolated to time $t = 0$.

The measurements were performed on powder, polycrystalline and single crystal materials as a function of temperature, orientation and external field. At a first glance one might expect that the muon precession in zero external field is, due to the statistical distribution of the local field directions, not observable. This is true for $\theta = 90°$ or at right angles to the beam polarization (Fig. 2). For $\theta = 0°$ (180)° it is easily seen that the muon precessing around any of the local field axes will after integer multiples of the Larmor period always point in the beam direction. Thus the maximum of the positron counting rate will always be observed in multiples of the Larmor time, independent of the arbitrary field direction. The asymmetry observed in a ferromagnetic powder sample in zero external field is reduced to $\frac{2}{3}$ of the value measured for a non-magnetic sample in a transverse field. Figure 7 shows as an example the μSR spectrum observed in a Co single crystal at zero field.

In the following, the various contributions to B_μ will be discussed [7].

The hyperfine field, $\vec{B}_{hf}(\vec{R}_\mu)$ results from the interaction with the polarized conduction electron cloud around the muon at site $\vec{R}_\mu$ and is given by

$$B_{hf,i}(\vec{R}_\mu) = \int d^3r D_{ij}(\vec{r} - \vec{R}_\mu) M_j(\vec{r}). \tag{11}$$

Here $\vec{M}(\vec{r})$ is the conduction electron magnetization and

$$D_{ij}(\vec{x}) = (\nabla_i \nabla_j - \tfrac{1}{3}\delta_{ij}\Delta)\frac{1}{x} - \frac{2}{3}\delta_{ij}\Delta\frac{1}{x}. \tag{12}$$

The first term in (12) transforms as a spherical harmonic of order 2. Therefore, for a spherically symmetric screening cloud, only the second term contributes to the hyperfine field. This yields the contact field

$$\vec{B}_{hf}(\vec{R}_\mu) = \tfrac{8}{3}\pi\vec{M}(\vec{R}_\mu). \tag{10}$$

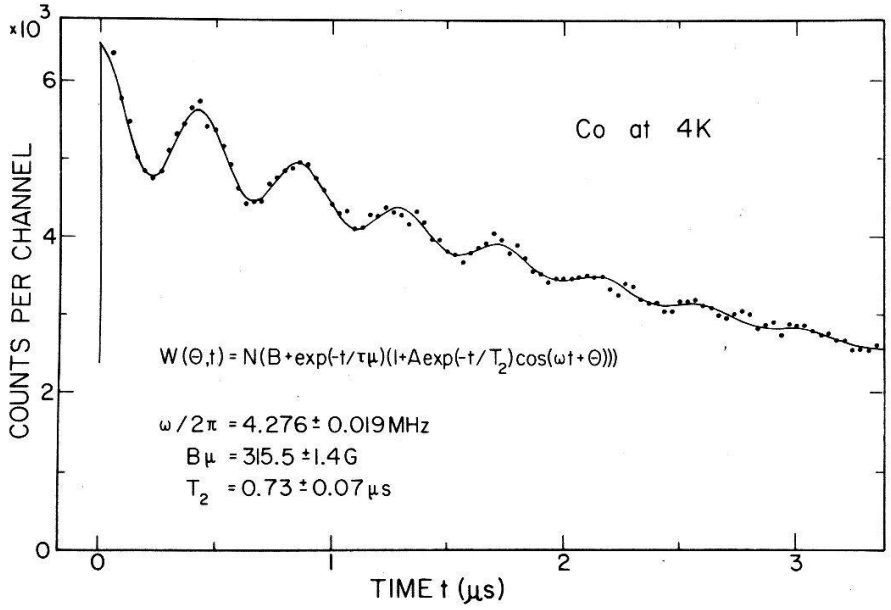

Figure 7
μSR spectrum of the Co single crystal at 4 K in zero external field. From the fit of this time spectrum $|B_\mu|$ and T_2 were obtained.

Other contributions may arise from the non-spherical parts of the screening cloud. They would give rise to a pseudo-dipolar field contribution to the hyperfine field since they have the same symmetry properties as the dipolar field discussed below but are of short range only.

The dipolar interaction with all magnetic moments $\vec{\mu}(\vec{m})$ localized at the lattice sites $\vec{m}$ gives rise to the dipolar field $\vec{B}_{\rm dip}(\vec{R}_\mu)$:

$$B_{{\rm dip},i}(\vec{R}_\mu) = \sum_{\vec{m}} D_{ij}(\vec{m} - \vec{R}_\mu)\mu_j(\vec{m}), \tag{13}$$

where D_{ij} is given by equation (12) except that we may neglect here the contact terms since the μ^+ is assumed to avoid the occupied lattice sites $\vec{m}$.

If the direction of the localized magnetic moments varies periodically in space, as is the case for an antiferromagnetic or helical spin arrangement, the sum (13) over an infinite lattice is convergent. The dipolar field at the muon may then be obtained by extending the sum over the lattice sites $\vec{m}$ of the sample to a sum over an infinite lattice. The calculation of the latter sum is discussed in Appendix B. Thus for the case of the zero field measurement in *Dy* which has a helical spin structure for temperatures between 85 K and 179 K the local field is

$$\vec{B}_\mu(\vec{R}_\mu) = \vec{B}_{\rm dip}(\vec{R}_\mu) + \vec{B}_{\rm hf}(\vec{R}_\mu) \tag{14}$$

with $B_{\rm dip}$ and $B_{\rm hf}$ given by equations (10) and (13).

For a ferromagnetic alignment of the localized moments, the dipolar sum (13) over an infinite lattice is only conditionally convergent. For a finite sample, this means that the sum is shape dependent. The usual procedure is first to sum over all dipoles within a volume Ω around $\vec{R}_\mu$ and to replace the sum over the

remaining volume $V-\Omega$ by an integration:

$$B_{\mathrm{dip},i}(\vec{R}_\mu)=\sum_{\vec{m}\in\Omega} D_{ij}(\vec{m}-\vec{R}_\mu)\mu_j(\vec{m}) + \frac{N}{V}\int_{V-\Omega} d^3r D_{ij}(\vec{r})\mu_j(\vec{r}). \tag{15}$$

The first part results in a contribution $\vec{B}'_{\mathrm{dip}}(\vec{R}_\mu, \Omega)$, the residual dipolar field, which depends on the lattice structure, the muon site, and the volume Ω. By partial integration, the second part is transformed into two surface integrals. The value from the inner surface is dependent on the volume Ω and is called the Lorentz field $\vec{B}_{\mathrm{L}}(\Omega)$. If this volume is chosen to be a sphere around $\vec{R}_\mu$ (as will be the case in the actual calculations of $\vec{B}'_{\mathrm{dip}}$ performed in Appendix B), the value of the Lorentz field is

$$\vec{B}_{\mathrm{L}}=\frac{4\pi}{3}\vec{M}_{\mathrm{s}}, \tag{16}$$

where $\vec{M}_{\mathrm{s}}$ is the magnetization of the single domain in which the muon is located. By symmetry, for a spherical Ω volume the residual dipolar field sum $\vec{B}'_{\mathrm{dip}}(\vec{R}_\mu, \Omega)$ is independent of Ω if the radius of the sphere is chosen large enough. The integral from the outer surface depends on the state of magnetization of the sample. For zero net magnetization, the contributions from the differently aligned domains cancel each other. If an external field is present, we obtain the shape-dependent demagnetization field $\vec{B}_{\mathrm{dem}}(V, \vec{B}_{\mathrm{ext}})$. For ferromagnetic materials, the dipolar field interaction of the muon with the localized moments of the sample can thus be split into the contributions:

$$\vec{B}_{\mathrm{dip}}(\vec{R}_\mu)=\vec{B}'_{\mathrm{dip}}(\vec{R}_\mu)+\vec{B}_{\mathrm{L}}+\vec{B}_{\mathrm{dem}}. \tag{9}$$

The values of the residual dipolar field, $\vec{B}'_{\mathrm{dip}}(\vec{R}_\mu)$, are further discussed in Appendix B for various lattice structures and muon sites $\vec{R}_\mu$. Here we just note that $\vec{B}'_{\mathrm{dip}}(\vec{R}_\mu)$ can be expressed as

$$B'_{\mathrm{dip},i}(\vec{R}_\mu)=E'_{ij}(\vec{R}_\mu)\mu_j, \tag{17}$$

where the dipolar tensor $E'_{ij}(\vec{R}_\mu)$ is symmetric and traceless. This implies that the residual dipolar field is zero if the magnetic moments have an arrangement which is of cubic symmetry with respect to $\vec{R}_\mu$. This applies to both octahedral and tetrahedral interstitial sites (as well as to substitutional sites) in fcc lattices.

IV. μSR in cobalt

The transition metal Co is ferromagnetic below the Curie temperature $T_{\mathrm{C}}=1395$ K. Co has the hexagonal-closed-packed (hcp) structure below 690 K and the face-centered-cubic (fcc) structure above 690 K. Since in polycrystalline Co both phases may coexist, only single crystal samples were used. The saturation magnetization densities measured [8, 9] and extrapolated to 0 K have been found to be 1415 G for the hcp and 1446 G for the fcc phase. The corresponding magnetic moments are $1.71\mu_{\mathrm{B}}^{e}$ and $1.75\mu_{\mathrm{B}}^{e}$. Below 500 K the easy axis of

magnetization is the hexagonal axis. In the range from 500 K to 600 K the spin direction changes slowly from the c-axis into the basal plane [10].

1. *Measurements*

Basically, three types of measurements have been made on single crystal cobalt: (a) precession frequency measurements of the muon as a function of temperature in zero external field, (b) a separate experiment to determine the sign of the local magnetic field at the muon site, and (c) the external magnetic field dependence of the local magnetic field at room temperature and at 875 K. In all measurements the depolarization time is obtained in the fit to the time histogram. For the zero field measurements an oriented ellipsoidal single crystal 12 mm long and 8 mm in diameter was used. The external field measurements were performed on an 8 mm diameter single crystal sphere. Preliminary results of these measurements were reported earlier [11].

(a) *Zero field measurements*

Figure 8 shows the effective magnetic field, $|B_\mu|$, as a function of temperature in zero external field. These measurements must be interpreted in three temperature regions. The low temperature region below 450 K shows with increasing temperature a smooth decrease in the absolute local field $|B_\mu|$ from 315 G to 100 G. The signal disappears at 520 K probably due to field inhomogeneities in the sample, but returns again at 550 K. From 550 K to 680 K the local field increases continuously from 180 G to 400 G. The muon frequency shows a jump from 400 to 740 G, indicating a local field discontinuity at 690 K, the temperature for the crystal structure change. From this point to the highest temperature measured the muon frequency remains approximately constant.

The depolarization time is represented in Fig. 9 as a function of temperature. The depolarization time at 4 K is about 0.8 μs and remains approximately constant up to 350 K. This time decreases to an almost unobservably short value in the spin rotation region and then increases to 1.2 μs at 100 K. The observed

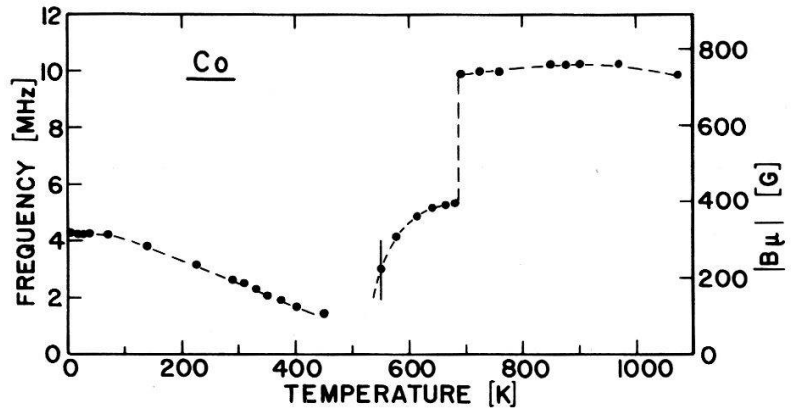

Figure 8
Temperature dependence of the μSR precession frequency for single crystal Co in zero external field. The errors of the points are smaller than the plotted points, except at $T = 550$ K. The right-hand scale gives the absolute value of the local field B_μ corresponding to the μSR frequency.

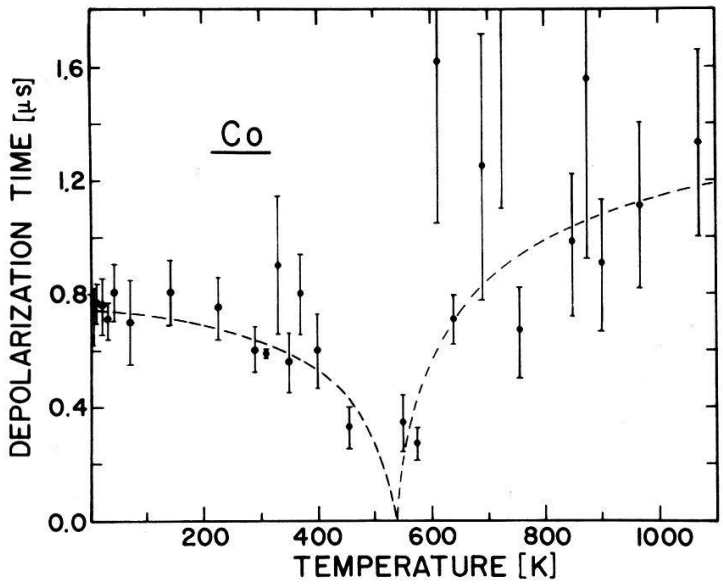

Figure 9
Temperature dependence of the depolarization time for the μSR signal in Co single crystal. Near 550 K the depolarization time becomes very short, probably due to field inhomogeneities. The dashed line indicates the general trend.

decrease of the depolarization time in the spin rotation region is probably due to field inhomogeneities in the sample.

The asymmetry A_{eff} was found to be 0.10 ± 0.04 independent of temperature. The reduction from the expected value of ≈ 0.25 is mainly due to background effects resulting from muons stopped in the dewar (oven) walls.

(b) *Sign determination of B_μ in cobalt*

In order to understand the contributions to the resultant local magnetic field in Co it is necessary to determine the sign of B_μ. The alteration of the local field brought about by an external field above the saturation value was hampered by technical problems. The rather small spherical sample requires an external field for saturation ($(4\pi/3)M_s$) in excess of 6 kG. In addition to the fact that this field exceeds the limit of our Helmholtz magnet pair, this high field causes a significant energy dependent bending of the decay positron trajectories, which results in a considerable decrease in counting rates.

The sign of B_μ may be determined directly by measuring the sense of the muon precession when an external field is applied. The precession direction can be obtained by analysing the relative phase of the signals produced by the decay positrons in the two scintillator counters forward and perpendicular to the beam direction (see Fig. 4). In zero external field the muon precession is not observed in the perpendicular detector since the average field in the unmagnetized sample is zero. With the application of an external field, however, the fraction of domains magnetized along the external field will increase and a larger fraction of the muons stopped in the sample will precess about a given direction resulting in a signal observable in the perpendicular counter.

A phase determination requires an exact knowledge of zero time in the forward and perpendicular detector. In order to partially circumvent this problem

of determination of the zero time directly a non-magnetic reference sample was used for comparison.

In this experiment the reference signals were obtained at high temperatures from the walls of the oven containing the sample. At lower temperatures non-magnetic materials were used in place of the cobalt sample. In order to minimize inaccuracies due to the poorly known zero time the reference frequency was adjusted to be close to the frequency of the muon in cobalt. In the high temperature region (875 K) an applied field of 1 kG was used to produce the reference signal. At the low and intermediate temperatures (673 K and 293 K) a field of 4.5 kG was used which clearly separated the cobalt signal from muons stopped outside the sample. For these measurements it is necessary to orient the crystal so that the cobalt spins are perpendicular to the incoming muon polarization. The results of the fitting procedure for the Co and reference signal are given in Table I. In each temperature region the fitted phases were compared as $\delta_{Co} = \theta_{Co}(\text{forw.}) - \theta_{Co}(\text{perp.})$ and $\delta_{ref} = \theta_{ref}(\text{forw.}) - \theta_{ref}(\text{perp.})$. The ratio $r = \delta_{Co}/\delta_{ref}$ is $+1$ for B_μ in the same direction as the magnetization and -1 for B_μ oppositely directed. Table I shows that at 293 K B_μ is negative with respect to the bulk magnetization. In both the fcc and hcp phases above the spin rotation region the muons are observed to precess with the same sense as those of the reference, i.e. $B_\mu > 0$. Various arguments may be advanced to explain the deviation of r from 1. The errors given in Table I include only fitting errors due to statistics, but no systematic errors such as crystal orientation, frequency difference effects between the Co and reference, differing positron trajectories in different fields etc. It is believed that the results of the sign determination of B_μ in the various temperature regions may be accepted with a rather high confidence level. Additional substantiation of these signs will come from other experiments described below.

(c) *External field dependencies*

The external field dependence of the muon precession frequency was measured in both the hcp and fcc phases. The hcp measurements were made at room temperature and the fcc measurements at 875 K. The results of these measurements are shown in Fig. 10. Four different cases were investigated: (1) The local field in the fcc phase was found to be independent of the external field applied along a random direction. (2) B_μ is also independent of the external field when the external field is applied along the c-axis in the hcp phase. (3) B_μ shows a strong external-field dependence, however, when the external field is applied perpendicular to the c-axis in the hcp phase. (4) With the external field applied at an angle of 45° to the c-axis B_μ increases with a smaller slope. The striking result that for case (1) and (2) B_μ is independent of B_{ext} and that B_μ depends on the angle between B_{ext} and the c-axis in the hcp phase will be discussed below.

2. *Discussion*

(a) *Muon site and hyperfine fields*

The relevant information to be obtained from the data is the site of the stopped muon and the various contributions to the local field which the muon

Table I
Sign of the local field B_μ in Co.

Temp. [K]	Sample	B_{ext} [G]	θ_{Det} [rad]	A_{eff} [%]	T_2 [μs]	ν [MHz]	θ_{Fit} [rad]	$\delta = \theta_0 - \theta_{\pi/2}$ [rad]	$r_{exp} = \delta_{Co}/\delta_{ref}$
293	Co	4500 $\parallel \hat{c}$	0 (=forw)	8.2±0.6	0.28±0.02	2.60±0.06	+0.12±0.06	−0.63±0.11	−0.47±0.08
		"	$\pi/2$ (=perp)	13.4±1.4	0.21±0.02	2.82±0.08	+0.75±0.09		$\rightarrow B_\mu < 0$
	ref	200	0	16.7±0.03	>10	2.78±0.01	+0.53±0.03	+1.35±0.06	
		"	$\pi/2$	22.5±0.01	>10	2.80±0.01	−0.92±0.05		
673	Co	4500 $\perp \hat{c}$	0	0.6±0.2	4.0 ±6.7	5.84±0.23	+0.09±0.42	+0.61±0.50	+0.41±0.34
		"	$\pi/2$	2.2±0.1	0.27±0.10	6.14±0.23	−0.52±0.27		$\rightarrow B_\mu > 0$
	ref	400	0	14.4±0.2	1.24±0.03	5.39±0.05	+0.26±0.02	+1.50±0.04	
		"	$\pi/2$	16.5±0.5	1.38±0.11	5.37±0.01	−1.24±0.03		
875	Co	1000	0	5.1±0.1	2.33±0.91	10.33±0.04	−0.02±0.12	+1.59±0.70	+0.92±0.42
		"	$\pi/2$	5.8±0.3	0.59±0.42	10.46±0.37	−1.61±0.69		$\rightarrow B_\mu > 0$
		1000	0	14.0±1.0	0.29±0.03	13.32±0.05	−0.25±0.08	+1.72±0.17	
		"	$\pi/2$	16.0±3.0	0.37±0.08	13.23±0.09	−1.97±0.15		

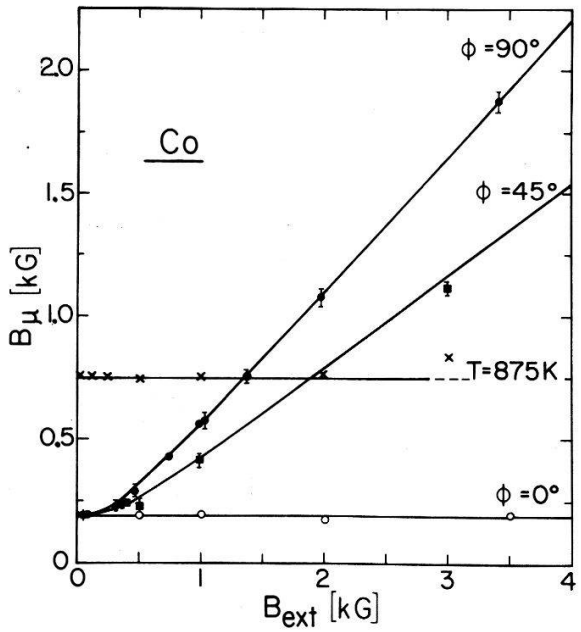

Figure 10
External field dependence of the local field B_μ for a spherical single crystal of Co. For the two cases, i) the cubic high-temperature phase ($T = 875$ K) and, ii) for B_{ext} parallel to the c-axis, ($\Phi = 0°$), at room temperature, one observes that the local field B_μ is independent of B_{ext} below saturation. For B_{ext} perpendicular ($\Phi = 90°$) and $\Phi = 45°$ with respect to the c-axis, B_μ increases with B_{ext}. The lines drawn for these two angles represent a fit through the data points with the result that $K_1 = +(4.8 \pm 0.3) \times 10^6$ erg/cm^3 under the assumption that the octahedral site is the stopping site and $K_1 = (5.7 \pm 0.3) \times 10^6$ erg/cm^3 for an assumed tetrahedral site.

sees. The difficulty is that these two questions are interrelated and one must try to solve the problem such that a consistent picture develops. Recall that in the absence of an external field the field at the muon site is given as

$$\vec{B}_\mu = \frac{4\pi}{3}\vec{M}_s + \vec{B}'_{dip} + \vec{B}_{hf}. \tag{9}$$

The saturation magnetization was calculated as $M_s = \rho(T)\sigma_{sT}$, where σ_{sT} is the saturation magnetization per unit mass at 0 K and the temperature T, and $\rho(T)$ is the sample density. The density as a function of temperature has been calculated from known lattice parameters [12, 13]. To a good approximation one gets for $T < 290$ K:

$$\begin{aligned} a(T) &= (2.5014 + 0.56074 \times 10^{-7} T^2)\ \text{Å} \\ c(T) &= (4.0583 + 0.15672 \times 10^{-6} T^2)\ \text{Å} \end{aligned} \tag{18}$$

and for $T > 290$ K:

$$\begin{aligned} a(T) &= (2.4980 + 2.5939 \times 10^{-5} T + 6.6289 \times 10^{-9} T^2 \\ &\quad + 1.4328 \times 10^{-13} T^3)\ \text{Å} \\ c(T) &= (4.0523 + 6.3357 \times 10^{-5} T + 1.0448 \times 10^{-8} T^2 \\ &\quad + 1.2004 \times 10^{-12} T^3)\ \text{Å}. \end{aligned}$$

The magnetization σ_{sT} is well represented by

$$\sigma_{sT} = 1446(1. - 1.9 \times 10^{-10} T^3)\ \text{G} \tag{19}$$

between 0 K and 700 K.

For a light particle, there are two natural interstitial sites in an hcp crystal, the tetrahedral and octahedral sites (see Fig. 15). It is also possible that the μ^+ is trapped at a cobalt vacancy. Therefore the dipole field B'_{dip}, was calculated for the tetrahedral and the octahedral interstitial sites as well as the substitutional site from equation (B14) using the above values for c and a as a function of temperature. For an arbitrary spin direction θ with respect to the c-axis

$$\vec{B}'_{dip}(\theta) = \mu(\sin\theta\, E'_{xx}\hat{i} + \cos\theta\, E'_{zz}\hat{k}). \tag{20}$$

This implies that in the temperature range 0 K to 500 K the dipole field is parallel to the c-axis. However, in the region of spin reorientation (500 K − 600 K) θ changes and both x and z components must be considered. The values of θ were obtained from neutron measurements [10] and were used in the calculation of the local dipole field. Above 600 K the magnetization and dipole fields lie in the basal plane of the hcp crystal.

The hyperfine field depends on the signs of the measured local field B_μ, and the site dependent dipolar field B'_{dip}, $(\vec{B}_{hf} = \vec{B}_\mu - \vec{B}_L - \vec{B}'_{dip})$. In Fig. 11 the hyperfine field is plotted for the various possible site and field combinations. The dipole fields, B'_{dip}, for the three possible sites (octahedral interstitial, tetrahedral

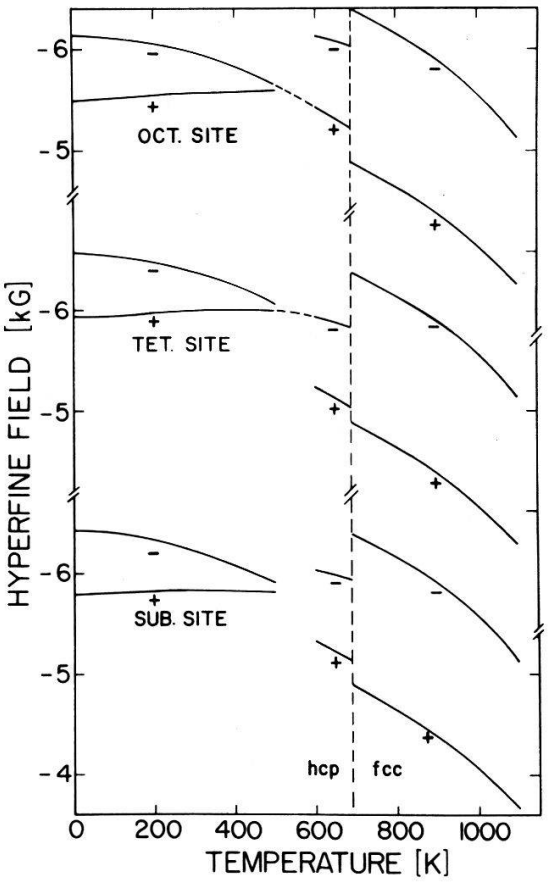

Figure 11
Calculated hyperfine field as a function of temperature for the various possible muon stopping sites combined with the assumed direction of $\vec{B}_\mu$ with respect to the magnetization, positive (+) for $\vec{B}_\mu$ parallel and negative (−) for $\vec{B}_\mu$ antiparallel to $\vec{M}$. Under the assumption that B_{hf} varies smoothly with temperature and follows approximately the Co magnetization curve, the figure suggests the octahedral site is occupied with B_μ negative at low temperature, and positive above the spin rotation region.

interstitial, and substitutional) are calculated and together with the Lorentz field are combined with B_μ under the assumption of a positive (+) or negative (−) direction of B_μ with respect to the direction of bulk magnetization. If the assumption is made that B_{hf}, the hyperfine field at the site of the muon should at least vary in a smooth manner then only two combinations are possible below 690 K, namely: the octahedral site under the condition that the sign of B_μ is negative at low temperatures and becomes positive above the spin rotation, or the tetrahedral site under the assumption that B_μ is positive below the spin rotation region and becomes negative above the transition. One might argue that the octahedral case is more plausible since the hyperfine field follows the magnetization curve rather well while for the tetrahedral case there is an unexplained increase in the absolute value of the hyperfine field with temperature. Further, the discontinuous change in the hyperfine field across the structural phase transition, which exists for both site possibilities is smaller for the octahedral case than that for the tetrahedral case.

The designation of the muon site is open to some question based on the results of the precession frequency alone and for this reason the experiment to determine the sign of B_μ through the precession sense was performed. The results shown in Table I show rather convincingly that the muon is precessing in cobalt in the opposite direction to that of the reference sample in the temperature region between 0 K and 500 K. For this to occur the local field B_μ is opposite to the bulk magnetization and hence opposite to the Lorentz field. Under the assumption that the hyperfine field should vary smoothly the only possibility for the muon site is the octahedral site.

In the fcc phase above $T = 690$ K, the site symmetry of the stopped muon can only allow a zero dipolar field. Therefore, one may obtain the hyperfine field directly as $\vec{B}_{hf} = \vec{B}_\mu - \vec{B}_L$.

Figure 12 summarizes the various contributions to the hyperfine field ($\vec{B}_{hf} = \vec{B}_\mu - \vec{B}_L - \vec{B}'_{dip}$). B_{hf} is negative and shows an unexplained large jump of 6% at the hcp-fcc phase transition. The discontinuity of the Lorentz field (including the density corrections [12, 13] accounts for only 1.8%. In addition to the large discontinuity at the phase transition B_{hf} varies in the hcp phase more strongly with temperature than the saturation magnetization. The hyperfine field measured via the μSR technique may be compared with neutron diffraction experiments [14, 15], which measure the distributions of the magnetic moments. From these measurements it is known that the spin density in the region between the cobalt atoms is indeed negative. In the hcp phase the magnetic form factors do not change with temperature [14] whereas in the fcc phase there is a possibility that the spin density at a site near the cobalt does change with temperature [16]. The exact nature of the spin distribution across the phase change is not known although it is clear from the magnetic moment measurements that some redistribution must take place. The presence of the positively charged muon may cause additional modifications in the spin density across the phase change.

(b) *External field dependence*

The internal field within a magnetic domain as a function of applied field is a result of the interplay between the various contributions to the total magnetic energy in the system. The relevant quantities in Co are the demagnetization

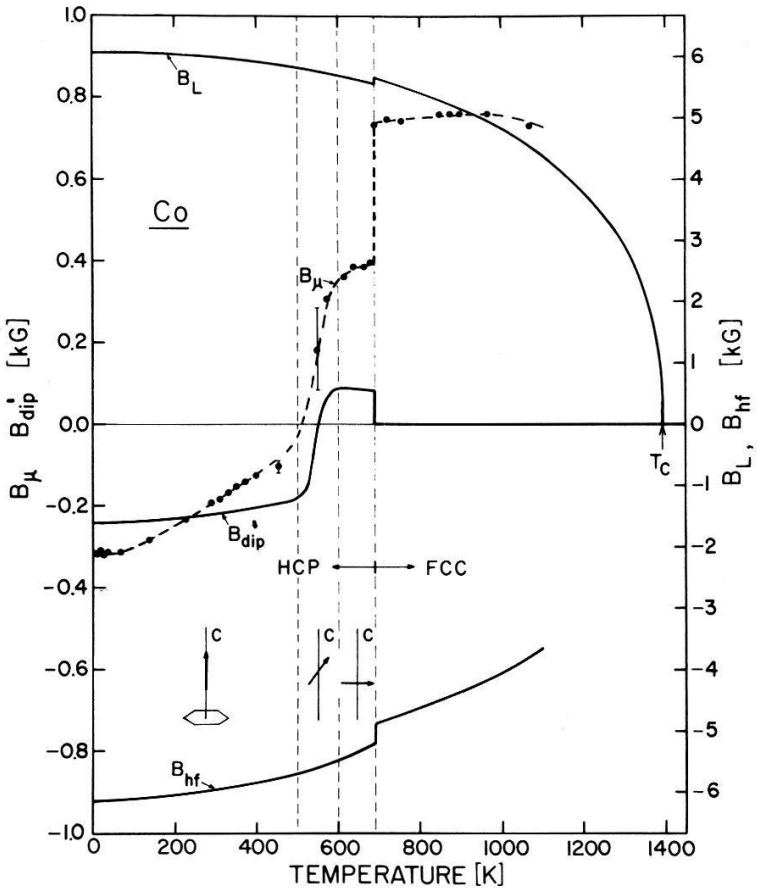

Figure 12
The temperature dependence of the measured local field B_μ and the contributions to B_μ in Co. The Lorentz field B_L and the dipolar field B'_{dip} were calculated as described in the text. The figure shows the projection of $\vec{B}'_{dip}$ along the local magnetization direction. The hyperfine field B_{hf} was computed from the measured values. The easy axis of magnetization changes in the temperature range 500 K to 600 K. A structural phase-change from hcp to fcc occurs at 690 K. The sign of the field components is defined with respect to the local magnetization, M_s, direction. Note the different scales for the various field components.

energy E_{dem}, the energy of a domain in an external field E_{ext}, and the anisotropy energy E_{ani}

$$E_{tot} = E_{dem} + E_{ext} + E_{ani}. \tag{21}$$

The competition between the external field and the anisotropy energy determines the angle θ which the spin takes in the crystal and thus effects the internal field. The demagnetization energy per unit volume is equal to $-\frac{1}{2}NM^2$. For a sphere $N = 4\pi/3$. The magnetic energy, E_{ext}, per unit volume for an external field B_{ext}, is given as $-MB_{ext}$ for a given domain. The anisotropy energy has its origin in the spin-orbit interaction in which the orbital angular momentum reflects the symmetry of the atomic site in the crystal [17]. Generally the anisotropy energy can be written $\sum_n K_n \sin^{2n} \theta$. For cobalt in the hcp phase it is sufficient to use

$$E_{ani} = K_1 \sin^2 \theta + K_2 \sin^4 \theta. \tag{22}$$

The spin direction is determined by minimizing the potential energy for each domain considered. In the absence of an external field this results in $\theta = 0°$ for the temperature region 0 K to 520 K, $\theta = 90°$ in the temperature region 600 K to

690 K, and $\sin^2\theta = -K_1/2K_2$ in the spin rotation region between 500 K and 600 K.

For measurements of hcp cobalt in the external field, it is necessary to consider the domain structure of cobalt. The size and direction of domains is again dictated by a minimization of the total energy. The particular case for hcp cobalt has been considered by Birss and Martin [18] using Néel's theory of phases [19]. Cobalt possesses a twofold magnetic symmetry because of the atomic arrangement at low and intermediate temperatures so that the magnetic directions are always parallel or antiparallel to the easy axis (c-axis) of magnetization. One may denote α as the fraction of the cobalt sample for which the domains lie parallel to the c-axis, then $(1-\alpha)$ is the fraction of domains antiparallel. As mentioned, the minimum energy may be obtained by minimizing the energy separately in both domains. Considering equation (21) and assuming that an external field is applied at an angle Φ_i with respect to the c-axis of a given domain ($i = 1, 2$) one may minimize the energy with respect to the spin angle θ_i obtaining

$$(2K_1 + NM_s^2)\sin\theta_i + 4K_2\sin^3\theta_i - MB_{\text{ext}}\sin\Phi_i = 0 \tag{23}$$

or in the case of cobalt, where $K_1 \gg K_2$

$$\sin\theta_i = (MB_{\text{ext}}\sin\Phi_i)/(2K_1 + NM_s^2). \tag{24}$$

Also for cobalt $\Phi_2 = \pi - \Phi_1$ so that $\theta_1 = \theta_2 = \theta$ and the total energy of the system may be written with the following contributions:

$$\begin{aligned} E_{\text{dem}} &= \tfrac{1}{2}N\{[\alpha M_s\sin\theta + (1-\alpha)M_s\sin\theta]^2 + [\alpha M_s\cos\theta - (1-\alpha)M_s\cos\theta]^2\} \\ E_{\text{ext}} &= -\alpha M_s B_{\text{ext}}\cos(\Phi-\theta) + (1-\alpha)M_s B_{\text{ext}}\cos(\Phi+\theta) \\ E_{\text{ani}} &= \alpha(K_1\sin^2\theta + K_2\sin^4\theta) + (1-\alpha)(K_1\sin^2\theta + K_2\sin^4\theta). \end{aligned} \tag{25}$$

The condition for minimization with respect to α gives

$$2\alpha - 1 = (B_{\text{ext}}\cos\Phi)/(NM_s\cos\theta). \tag{26}$$

Once the angle θ is known for a given external magnetic field the local field B_μ, in either domain can be calculated. Figure 13 shows the various field contributions with the resulting field given as

$$\vec{B}_\mu = \vec{B}_{\text{ext}} + \vec{B}_{\text{dem}} + \vec{B}_{\text{L}} + \vec{B}_{\text{hf}} + \vec{B}'_{\text{dip}}. \tag{8}$$

The net magnetization ($\vec{B}_{\text{dem}} = -N\vec{M}$) is a vector sum of the magnetization from each domain. The hyperfine fields are assumed to be parallel to M_s in either domain. Under these conditions the local field components for the two domains $(+, -)$ may be written as

$$\begin{aligned} B_\mu^{\perp} &= B_{\text{ext}}\sin\Phi - NM_s\sin\theta + \frac{4\pi}{3}M_s\sin\theta + B_{hf}\sin\theta + B'^{\perp}_{\text{dip}}(\theta) \\ B_\mu^{\parallel} &= B_{\text{ext}}\cos\Phi - NM_s(2\alpha-1)\cos\theta \\ &\quad \pm\left(\frac{4\pi}{3}M_s\cos\theta + B_{\text{hf}}\cos\theta + B'^{\parallel}_{\text{dip}}(\theta)\right). \end{aligned} \tag{27}$$

Using equation (26) it is observed that the first two terms in B_μ are zero, thus guaranteeing that the field $B_{\text{int}} = B_{\text{ext}} + B_{\text{dem}}$ is perpendicular to the c-axis. For a

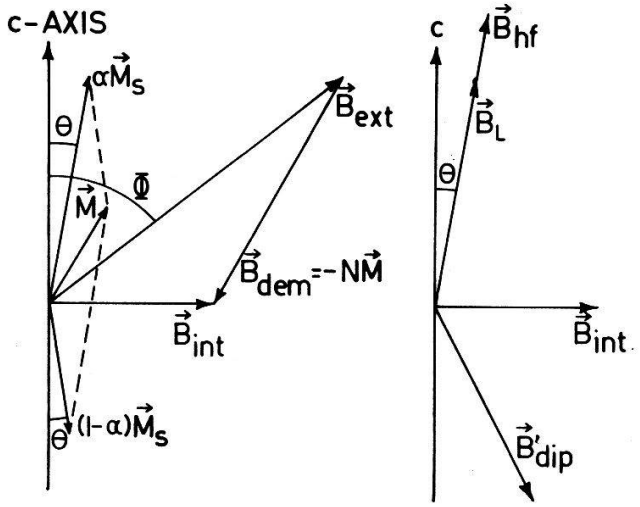

Figure 13
The various fields contributing to B_μ in an ellipsoidal single crystal of Co. The external field B_{ext} is at an angle Φ with respect to the c-axis (easy axis). The internal field is: $\vec{B}_{int}=\vec{B}_{ext}+\vec{B}_{dem}=\vec{B}_{ext}-N\vec{M}$, where $\vec{M}$ is proportional to the vector sum of the moments $\alpha\vec{M}_s$ and $(1-\alpha)\vec{M}_s$ from the two possible domains. As shown in the text $\vec{B}_{int}$ is perpendicular to the c-axis. On the right-hand side the contributions to $\vec{B}=\vec{B}_{hf}+\vec{B}_{int}+\vec{B}'_{dip}+\vec{B}_L$ are shown for one domain. $\vec{B}_{hf}$ is assumed to be parallel (or antiparallel) to the domain magnetization.

sphere ($N=4\pi/3$) equation (27) gives

$$B_\mu^\perp = B_{ext}\sin\Phi + B_{hf}\sin\theta + B'^{\perp}_{dip}(\theta)$$
$$B_\mu^\parallel = \pm\left(\frac{4\pi}{3}M_s\cos\theta + B_{hf}\cos\theta + B'^{\parallel}_{dip}(\theta)\right). \tag{27a}$$

This equation combined with the dipolar field calculations (see Appendix B) and equation (24) gives with μ, the effective magnetic moment,

$$B_\mu^2 = \left(\frac{4\pi}{3}M_s + B_{hf} + \mu E'_{zz}\right)^2 + \left\{\left[(2K_1 + 3\mu E'_{xx}M_s)\Big/\left(2K_1 + \frac{4\pi}{3}M_s^2\right)\right]B_{ext}\sin\Phi\right\}^2. \tag{28}$$

The behaviour of B_μ with external field is clearly dependent on the type of site occupied (E'_{ii}) and the anisotropy constant K_1. Figure 10 shows the experimentally observed B_μ as a function of externally applied field for $\Phi=0°$, 45°, and 90°. A fit to the data assuming the octahedral interstitial site is occupied gives a value of $K_1=(4.8\pm0.3)\times10^6$ erg cm^{-3} for the field applied at 90° to the c-axis in the hcp crystal, whereas, for the assumption of the tetrahedral site a value of $K_1=(5.8\pm0.3)\times10^6$ ergs cm^{-3} is obtained. The fit to the data for the field applied at 45° to the c-axis agrees with the respective value of K_1 assumed correct from the 90° fit. Published values [20, 21, 22, 23] at room temperature vary somewhat, but as indicated in Table II are near the value 4.8×10^6 ergs/cm^3. The value 5.8×10^6 erg/cm^3 is outside the range of measured values. The external field measurements, therefore, give additional verification that the muon is sitting at the octahedral site in the hcp crystal.

Table II
Comparison of various literature values of the anisotropy K_1 with the μSR values of K_1 under the assumption of the tetrahedral (octahedral) interstitial site. The comparison gives additional evidence for the octahedral site.

K_1[erg/cm^3]	Method	Reference
5.3×10^6	Torque	19
4.3×10^6	Torque	20
4.4×10^6	Torque	21
5.2×10^6	Magnetization	22
4.8×10^6	average	19–22
$(4.8\pm0.3)\times10^6$	μSR (oct.)	
$(5.8\pm0.3)\times10^6$	μSR (tet.)	

The results for the fcc phase measurements indicating an independence of external field below 2.5 kG are to be expected since the B'_{dip} contribution is zero. If the local dipole contribution is zero then $\vec{B}_\mu = \vec{B}_{ext} + \vec{B}_{dem} + \vec{B}_{hf} + \vec{B}_L$. At external fields below saturation the first two terms cancel each other and therefore the internal field is determined solely by B_L and B_{hf}. [If the external field is greater than NM_s the internal field is affected.] For the cylindrical sample used the value of N is 1.72.

3. *Conclusions*

a) In the interpretation of the μSR results in cobalt it has been shown that the contribution to the local field from the local electronic magnetic dipoles must be taken into account. Calculations giving the correct B'_{dip} indicate that the electronic dipoles may be considered as localized.

b) Through the consideration of the local field contributions the muon site has been determined to be the octahedral interstitial site. This result represents the first unambiguous site determination for a free muon in a solid. From the results of these experiments it cannot be established whether the muon diffuses among the identical octahedral interstitial sites or is trapped on one.

c) From the external field measurements it is seen that the μSR method may be used to determine the magnetic anistropy energy coefficients K_i. The value of K_1 in hcp cobalt at room temperature is found to be $4.8\pm0.3\times10^6$ erg/cm^3.

d) The hyperfine field has been determined in this study as a function of temperature (Fig. 12). In cobalt an unexplained large discontinuity has been observed at the crystal phase transition. Additionally, it has been observed that the hyperfine field does not follow the internal magnetization. These effects which may be partially due to the perturbation by the muon itself are highly interesting and are further discussed in Section IX.

V. μSR studies in gadolinium

Gadolinium is a rare earth metal which crystallizes in the hcp structure. Below the Curie point, $T_C = 292$ K, Gd is ferromagnetic with a saturation

magnetization density [24] at 0 K of 2010 G. The magnetic moment of Gd has been measured by neutron diffraction [25] and found to be 7.55 μ_B^e at 4.2 K. The increase of 0.55 μ_B^e over that expected for $S=\frac{7}{2}$ has its origin in the exhange interaction with the polarized conduction electrons. The spin direction for temperatures above 230 K is along the c-axis. Below 230 K the easy axis of magnetization makes an angle θ with the c-axis. There is considerable discrepancy in the literature [26, 27, 28, 29] as to the temperature-dependent angle θ. Previous measurements with μSR in Gd have been reported as a function of temperature and magnetic field [30]. In the interpretation of their results the influence of the local dipole field was not considered. As is clear from the case previously discussed with cobalt the influence of the local electronic dipoles on the field B_μ must be taken into account. Preliminary results of the SIN measurements on Gd were reported earlier [31].

1. *Measurements*

The μSR measurements were made on a polycrystalline Gd sample in zero external field between 25 and 300 K. The sample used was a 15 g disk which was annealed at 1435 K for about one hour in an argon atmosphere. The annealing which was repeated several times between the measurements had the effect of increasing the asymmetry. In Fig. 14 the results of the measurements of the muon precession frequency as a function of temperature are shown. Clearly, $|\vec{B}_\mu|$ does not follow the magnetization curve as was also the case with Co. This somewhat complicated relationship of local field as a function of temperature shows a continuous increase in local field from 55 K to 170 K and a rather sharp dip at 225 K near the temperature for which the spins become aligned along the c-axis.

The depolarization time remains essentially constant over the entire temperature range measured with a value near 0.10 μs. The asymmetry measured was also independent of temperature with a value of $A_{\text{eff}}=8\pm1\%$.

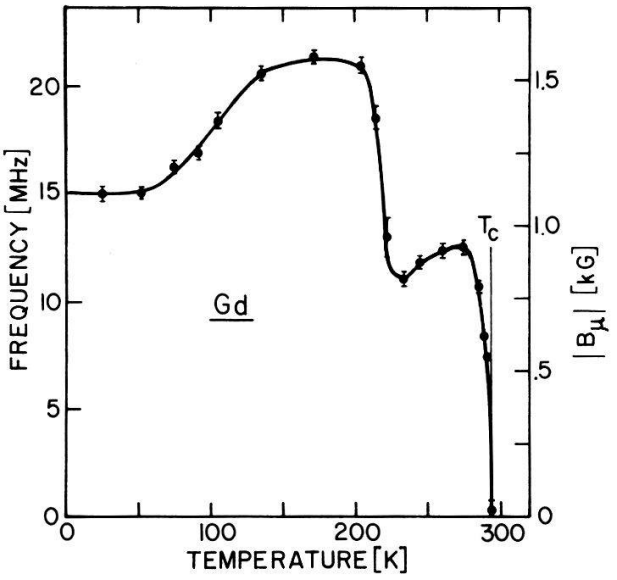

Figure 14
The absolute value of the measured local field B_μ vs. temperature in zero external field for polycrystalline Gd. The line drawn through the points serves as a guide to the eye.

2. *Interpretation and discussion*

In order to explain the observed temperature dependence of B_μ we must again consider the various field contributions responsible for the total internal field in the absence of an external magnetic field i.e.

$$\vec{B}_\mu = \vec{B}_L + \vec{B}'_{dip} + \vec{B}_{hf}. \tag{29}$$

B_L is given as usual as $(4\pi/3)M_s(T)$, where the known magnetization curve has been corrected for thermal expansion using the known temperature dependence of the lattice constants [32, 33]. The values at 0 K are $a = 3.628$ Å and $c = 5.795$ Å. In the hcp lattice the muon may stop at the octahedral or tetrahedral interstitial sites or may reside at a Gd vacancy.

The hcp structure of Gd is represented in Fig. 15 showing the possible interstitial sites. It is necessary to calculate the dipole field tensor, E'_{ij}, for these sites. The values may be obtained by using equation (B14), where again the temperature-dependence of a and c have been taken into account.

The complicated behaviour of the observed $\vec{B}_\mu$ with temperature must have its origin in the dipole field, $\vec{B}'_{dip}$, and in particular on the manner in which this field changes with the spin direction. The spins rotate from the c-axis at 230 K into a cone about the c-axis with varying angle θ as a function of temperature. Corner et al. [27] have expressed this anisotropy through the energy E_{ani} as

$$E_{ani} = K_1 \sin^2\theta + K_2 \sin^4\theta + K_3 \sin^6\theta. \tag{30}$$

The dipole field B'_{dip} transforms with spin direction as (see equation (B4))

$$B'_{dip} = \mu E'_{xx}(\sin\theta, 0, -2\cos\theta). \tag{31}$$

The value of μ is given as $7.55\ \mu_B^e(M_s(T)/M_s(0))$. In both the tetrahedral and octahedral interstitial sites as well as at the Gd vacancy site $E'_{zz} = -2E'_{xx}$. In determining the stop site of the muon, the fact that the dipole contribution $\vec{B}'_{dip}$

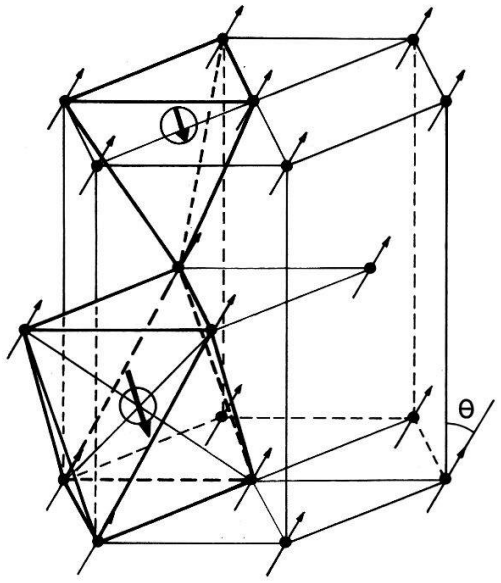

Figure 15
Dipolar fields at the tetrahedral and octahedral interstitial site in the hcp Gd lattice at 0 K. The Gd moments make an angle of $\theta = 30°$ with respect to the c-axis. The fields at the two sites are parallel to each other but not parallel to the Gd moments.

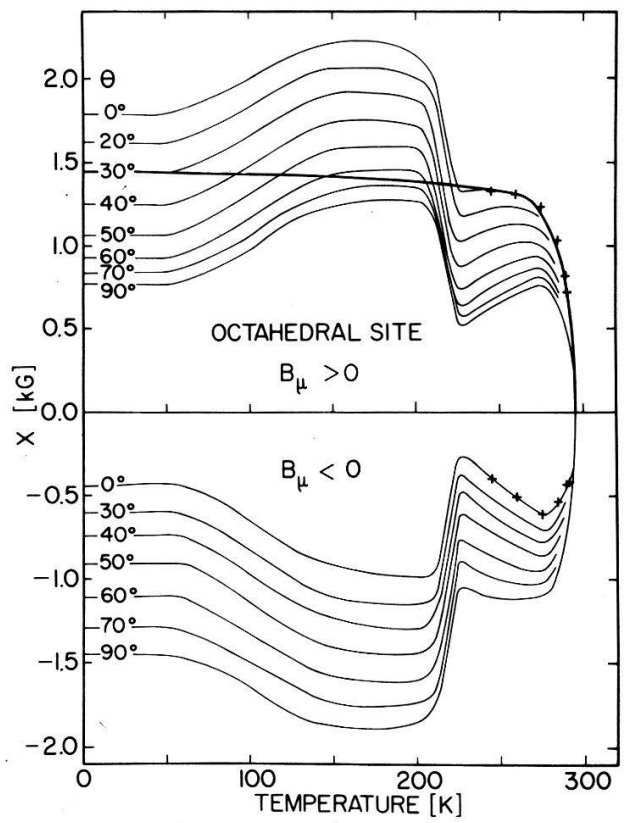

(a)

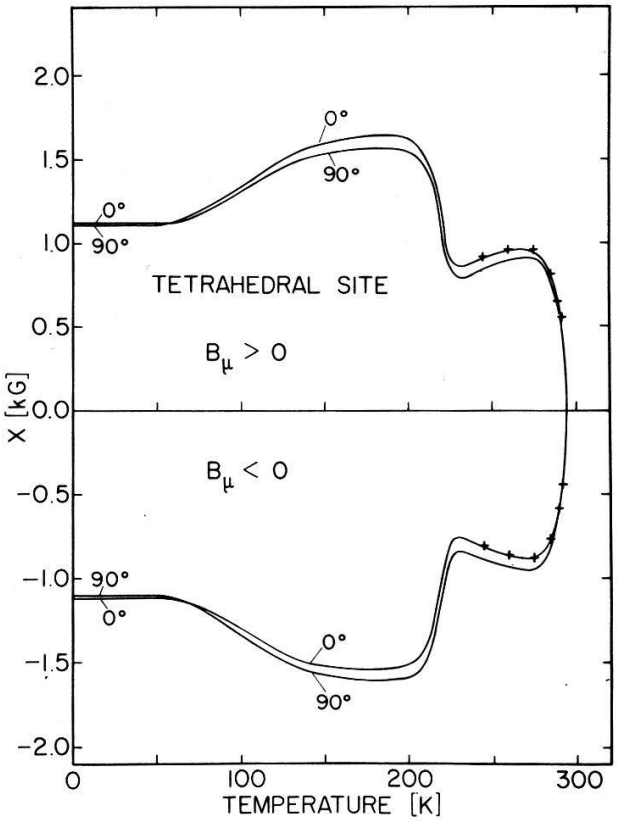

(b)

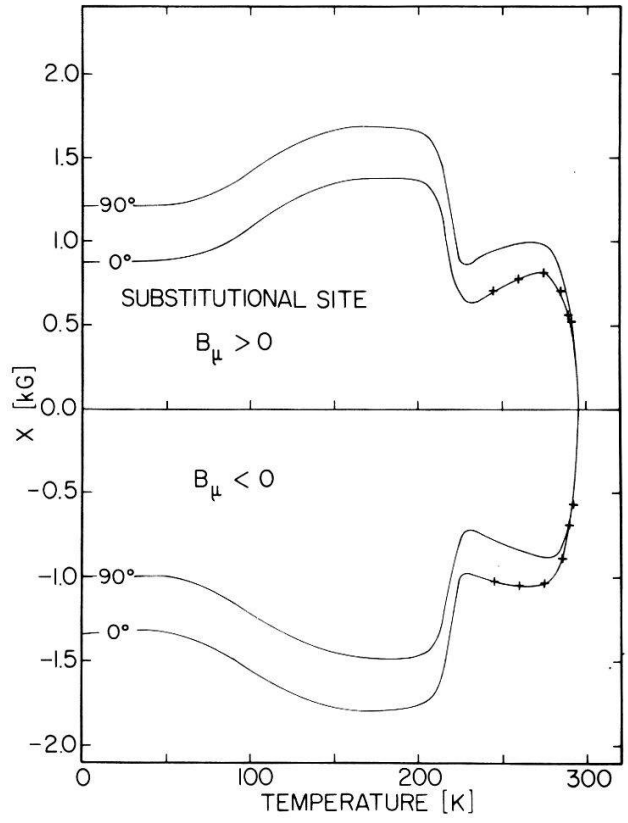

(c)

Figure 16

The field $\vec{X} = \vec{B}_\mu - \vec{B}_{\text{dip}} = \vec{B}_{\text{hf}} + \vec{B}_{\text{L}}$ is plotted as a function of temperature for three possible stopping sites (*a*, *b* and *c*) and for $B_\mu > 0$ and $B_\mu < 0$. From neutron diffraction and torque measurements it is known that $\theta = 0$ for $T > 230$ K. With this boundary condition and the assumption that X should vary in a continuous manner with temperature, it follows from these figures that the octahedral site must be the stopping site with $B_\mu > 0$. The crosses on the curves for $T > 230$ K are for the μSR data with the boundary condition $\theta = 0°$. From the curves corresponding to the octahedral site with $B_\mu > 0$ the angle θ is determined.

transforms differently with θ than either $\vec{B}_L$ or $\vec{B}_{hf}$ was used. Combining these latter two fields a vector $\vec{X}$ was formed:

$$\vec{X} = \vec{B}_L + \vec{B}_{hf} \tag{32}$$

which transforms under θ as

$$\vec{X} = X(\sin\theta, 0, \cos\theta). \tag{33}$$

Using equations (9, 31–33) one gets:

$$B_\mu^2 = X^2 + 2X_\mu E'_{xx}(1-3\cos^2\theta) + \mu^2 E'^2_{xx}(1+3\cos^2\theta). \tag{34}$$

This equation can be solved graphically by assuming a given stop site ($E'_{xx}(\vec{R}_\mu)$) and generating a set of curves $X(T)$ with θ as a parameter and using the measured values of $B_\mu(T)$. Such sets of curves are shown in Fig. 16. Since the sign of $B_\mu(T)$ in the polycrystalline sample cannot be determined, combinations using both plus and minus $B_\mu(T)$ are considered. If one assumes that the complicated structure of B_μ as a function of temperature arises from the variation of B'_{dip} with θ, then the quantity $\vec{X} = \vec{B}_\mu - \vec{B}'_{dip}(\theta) = \vec{B}_{hf} + \vec{B}_L$ should vary in a smooth manner. An attempt is made to draw a smooth curve through these generated curves which will then give the spin angle θ. The boundary condition is used that the experimental $X(T)$ must follow the generated curve for $\theta = 0°$ between the temperatures 230 K and the Curie point where it is known the spins are aligned along the c-axis. For the choice of the octahedral site and $B_\mu > 0$, for all temperatures a smooth curve can be drawn, whereas, for other sites and signs of B_μ such a curve is impossible, therefore showing the octahedral site with $B_\mu > 0$ is the muon site. Further, from this curve one can determine the cant angles θ, over the entire temperature range. It is observed that the spin angle at 0 K is $\theta = 30° \pm 3°$. The angles θ (T) determined from the μSR measurements along with those determined by neutron diffraction [28] and torque measurements [26, 27, 29] are shown in Fig. 17. Figure

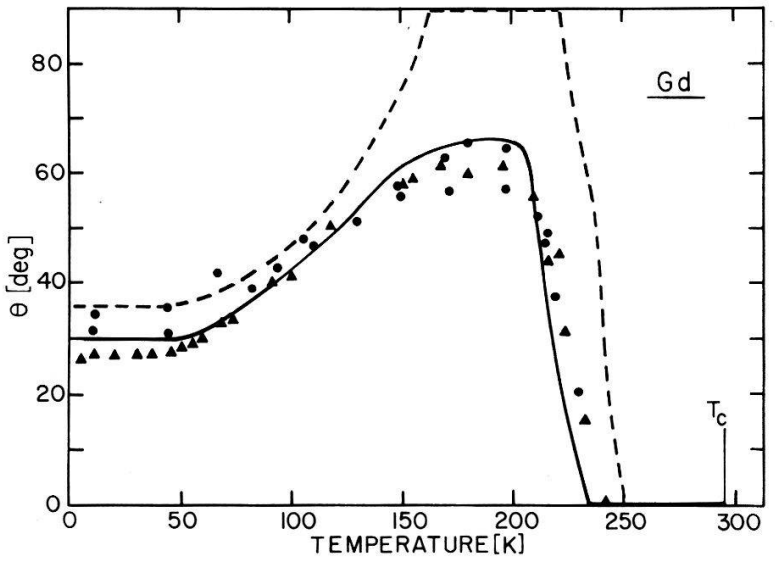

Figure 17
Plot of the angle between the magnetization and the c-axis as a function of temperature as extracted from μSR measurements (solid line). Indicated are also the values from neutron diffraction (●) (Ref. 28) and torque measurements (▲) (Ref. 26) and (– – –) (Ref. 29).

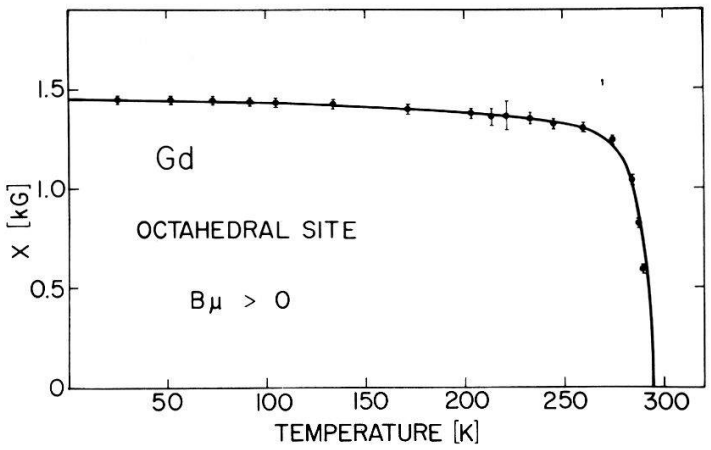

Figure 18
$\vec{X}(\theta, T) = \vec{B}_\mu(T) - \vec{B}'_{dip}(\theta)$ plotted against temperature. The angles $\theta(T)$, and therefore $\vec{B}'_{dip}(\theta)$, have been determined from the smooth fit of X indicated in Fig. 16a. The points with error bars are determined from the measured $B_\mu(T)$. The fact that the points are found to fall so well on the smooth $\vec{X}(\theta, T)$ curve indicates the model used, under the assumption of the muon stopping at the octahedral interstitial site with $B_\mu > 0$, is reasonable.

18 shows a separate plot of $X(\theta, T)$ versus temperature using the angles obtained from Fig. 17, where the actual measured values of $B_\mu(T)$ with the experimental error have been reinserted into equation (34). It is seen that the data fall quite well on the smooth curve $X(\theta, T)$ predicted under the assumption that the muon is in the octahedral site and that we have correctly accounted for the local field contributions.

Once the correct values of $X(T)$ have been established, the hyperfine field B_{hf} may be obtained as $\vec{B}_{hf} = \vec{X} - \vec{B}_L$ where B_L is given by $(4\pi/3)M_s(T)$. Figure 19 shows B_{hf} as a function of temperature together with the normalized magnetization curve. This deviation will be discussed further in Section IX.

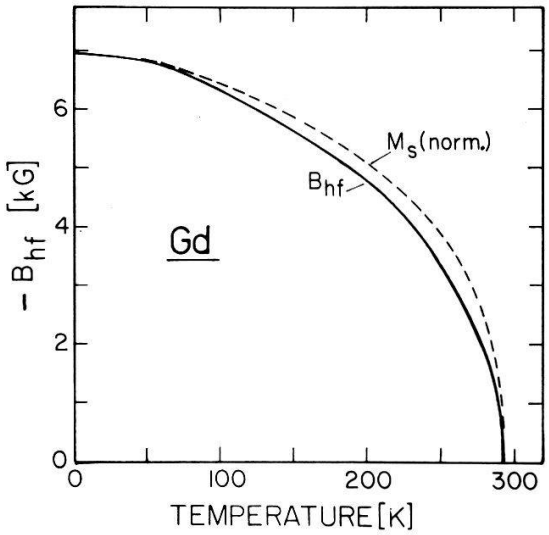

Figure 19
The extracted hyperfine field B_{hf} at the octahedral site in Gd is plotted as a function of temperature. The dashed curve is the magnetization data of reference [24] normalized to $B_{hf}(T = 0\,K)$. The hyperfine field is in this representation definitely below the magnetization curve. The hyperfine field is opposite (negative) to the local magnetization.

3. *Conclusions*

a) In the analysis of the Gd μSR data the importance of the dipole field B'_{dip} contribution to the local field has been shown. The calculated local field which changes with the spin rotation angle θ between 0 K and 230 K predicts the observed B_μ and therefore provides a means of obtaining θ from the μSR measurements. Further, the dipole calculation which correctly predicts the observed B_μ has been made under the assumption that the Gd magnetic moments are localized with the value 7.55 $\mu_B^e(M_s(T)/M_s(0))$.

b) Based on the correct analysis of the local field, the site of the muon has been shown in this polycrystalline sample to be the octahedral interstitial site.

c) The hyperfine field B_{hf} has been determined as a function of temperature and is shown to deviate from the normalized magnetization curve. The value for B_{hf} at 0 K is -6.98 ± 0.10 kG.

VI. μSR in dysprosium

Dysprosium is a rare earth metal with rather interesting magnetic properties. Between $T_N = 178$ K and $T_C = 85$ K, Dy is a helical antiferromagnet [34]. For this temperature range the spins lie in the basal plane of the hcp lattice with the axis of the helix parallel to the hexagonal axis. In this antiferromagnetic state the helix angle α, between the ferromagnetically ordered planes, is temperature-dependent, varying between 43° just below T_N to 26° at 90 K [35].

Below 85 K a discontinuous orthorhombic distortion occurs [36, 37] with a corresponding magnetic phase change to a ferromagnetic state. The spins are then found to lie again in the basal plane along the orthorhombic a axis [38, 39]. The magnetic moment has been measured to be 10.2 μ_B^e and the saturation magnetization at 0 K to be 2995 G [40].

In an earlier work [41] μSR measurements in Dy were reported. A drastic change in the amplitude and the relaxation time was observed in an external field as the sample was taken from the paramagnetic to the antiferromagnetic state. No measurements of the local field were performed, however. Preliminary results of the μSR measurements at SIN in Dy were reported earlier [42].

1. μSR *measurements*

The measurements were performed on an annealed polycrystalline disk with a diameter of 25 mm and a thickness of 5 mm. The results of the measurements of B_μ as a function of temperature are shown in Fig. 20. Signals are seen in both the antiferromagnetic and ferromagnetic states and within the accuracy of measurement vary in a continuous manner through the Curie temperature. The local field in the ferromagnetic state remains fairly constant. The asymmetry A, and the depolarization time T_2, have been determined and found to be essentially temperature-independent. The measured asymmetries are small ($\sim$0.03) and the relaxation time short, never longer than 200 ns.

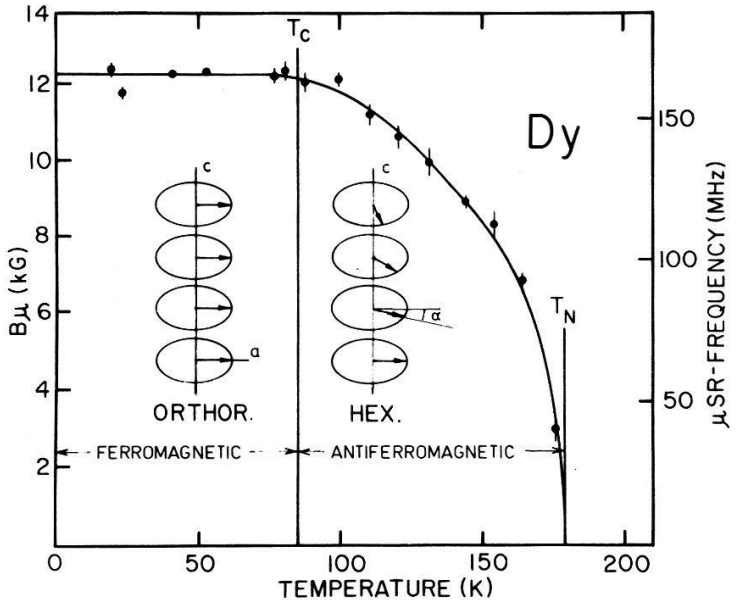

Figure 20
Temperature dependence of the local field B_μ for Dy in zero external field. T_C is the Curie temperature, T_N the Néel temperature. The spin structures in the ferro- and helical antiferromagnetic phases are indicated. Within experimental errors of about 1% no change of B_μ is seen at T_C.

2. *Discussion and results*

In the absence of an external field the internal field may be expressed as the sum of the hyperfine field and the total dipole field

$$\vec{B}_\mu = \vec{B}_{\rm hf} + \vec{B}_{\rm dip}. \tag{8}$$

In the ferromagnetic material one may consider $B_{\rm dip}$ to be composed of two components, the Lorentz field $B_{\rm L}$, and $B'_{\rm dip}$ the contribution due to magnetic dipoles within the Lorentz sphere. In the ferromagnetic phase $B'_{\rm dip} = \mu(T)E'_{xx}$. An exact calculation (see Appendix B) is needed to obtain E'_{xx} using the three orthorhombic lattice constants a, b, and c [36, 37]. It is assumed the spins lie along the a direction. The localized moment $\mu(T)$ was taken to be $10.2\,\mu_B^e(M_s(T)/M_s(0))$. The values of $M_s(T)$ were obtained from $\sigma(T)$ [40] corrected for density using the known lattice constants [33]. To a good approximation

$$M_s(T) = 2995(1.0 - 1.51\times10^{-5}T^2)\ \text{G} \tag{35}$$

from 0 K to 85 K.

For the case of the helical antiferromagnet it is necessary to calculate $B_{\rm dip} = \mu(T)E_{xx}$ as a single sum of dipole contributions over the crystal using equation (B4). The Ewald sum method which is optimized for convergence is described in Appendix B. The E_{xx} which depend on the interplane turn angle α, are calculated for the correct ratio $c/a = 1.58$ for the three possible muon stop sites in this hcp phase. The results of this calculation for the octahedral and tetrahedral interstitial site and the Dy substitutional site are shown in Fig. 40. The

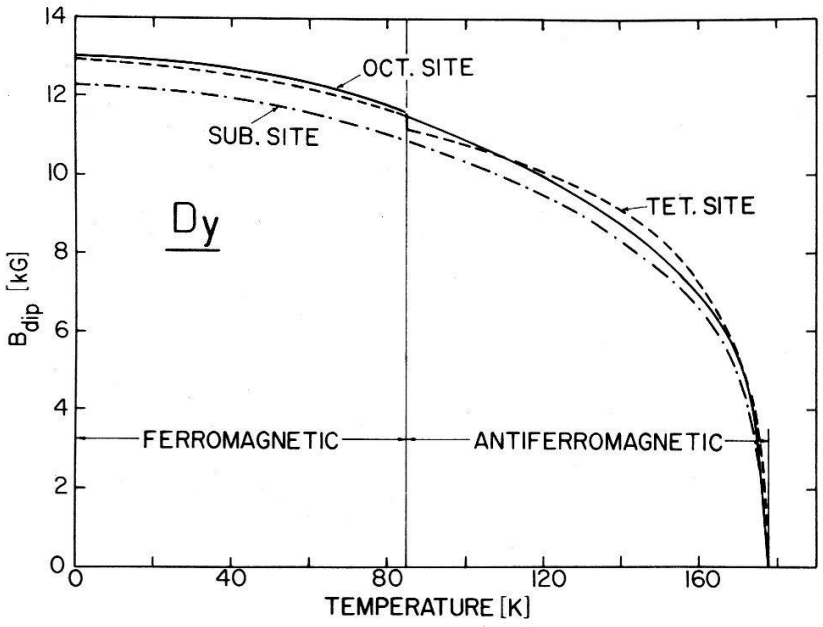

Figure 21
The calculated dipole fields B_{dip} in Dy under the assumption of three muon stop sites (octahedral interstititial, tetrahedral interstitial and Dy substitutional site). Although deviations do occur (~ 1 kG) the general shape of the curves with temperature are similar and the relative differences are small. It was not possible to determine experimentally which of these sites was occupied. It should be noted that in the ferromagnetic case B_{dip} was obtained as the sum of separately calculated B'_{dip} and B_L whereas, in the antiferromagnetic phase a single Ewald sum giving B_{dip} directly was made.

interplane turn angle can be well represented by

$$\alpha(T) = 14.6 + 0.101T + 0.00032T^2.$$

The magnetic moment in the antiferromagnetic phase is determined from $\mu(T) = 10.2\mu_B^e(M_s(T)/M_s(0))$, where the ratio $M_s(T)/M_s(0)$ was obtained from $B_{MB}(T)/B_{MB}(0)$ where $B_{MB}(T)$ is the measured hyperfine field at the nucleus as determined by Mössbauer data [43].

The results of the dipole field calculations B_{dip} for the three possible muon stop sites are shown in Fig. 21. It is of interest to note that the calculated dipole fields vary in an almost continuous manner across the phase change, although a discontinuity of 4% does exist for the calculated tetrahedral interstitial site case. Additionally, it is observed the dipole fields for the three sites do not differ greatly from one another.

Under the present experimental accuracy it is impossible to state definitely which calculated dipolar field as a function of temperature best fits the data. Since the muon has been shown to stop in the octahedral interstitial site in hcp Co and Gd, it is tempting to choose the octahedral interstitial site as the μ^+ stop site in Dy as well.

Assuming equation 8, B_{hf} may be extracted as the difference between B_μ and B_{dip}. Figure 22 shows B_{hf} so obtained under the assumption of the octahedral site for both positive and negative B_μ with respect to M_s. Since the calculated B_{dip} for the three possible stop sites do not differ significantly, the B_{hf} under the assumption of the tetrahedral interstitial site or the Dy substitutional site have not been represented. However, the curves for these sites appear quite similar. Under the assumption that $B_\mu < 0$, a large hyperfine field exists at 0 K (−25.35 kG) which has

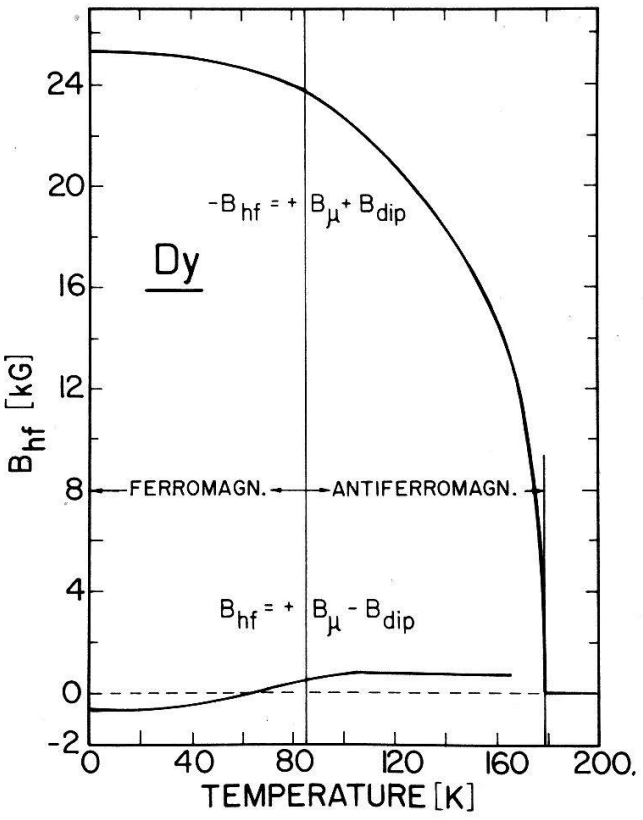

Figure 22
The resulting hyperfine field in Dy, $B_{hf} = \pm B_\mu - B_{dip}$, as a function of temperature. The curve shown is relatively insensitive to which particular B_{dip} is used (i.e. octahedral or tetrahedral interstitional site or substitutional site). For the case of a negative B_μ a rather large negative B_{hf} exists at 0 K, whereas, for a choice of a positive B_μ the hyperfine field is near zero over the entire measured temperature range.

the general form of the magnetization curve. For a $B_\mu > 0$ a much smaller hyperfine field is calculated which, within experimental accuracy can be considered temperature-independent and near zero (± 1 kG).

3. *Conclusions*

In the consideration of the μSR measurements on Dy the following conclusions may be drawn.

a) The muon precession frequency was observed in the anti-ferromagnetic phase of Dy. This represents the first observation of μSR in an antiferromagnetic metal.

b) The fact that the muon precession was observed in the antiferromagnetic phase can only be explained if the muon is not diffusing through the lattice.

c) A continuous variation of the muon precession frequency occurs across the magnetic and structural phase transition. Such an observation implies a continuous change in the local magnetic field across this transition region. This rather startling fact is, however, born out in the calculation of the local dipole fields as well.

d) It is not possible on the basis of these measurements to state unequivocally the particular stopping site of the muon. The dipole fields B_{dip} have been calculated for the tetrahedral and octahedral interstitial sites as well as for the

substitutional site. The difference in the local fields so calculated are not appreciably greater than the accuracy of the measurements. A preference might be argued for the octahedral site based on an expected similarity with the hcp materials Gd and Co where the stopping site of the muon is known.

e) The results of the hyperfine field in Dy as a function of temperature are shown in Fig. 22. Since it was not possible in this experiment to determine the sign of B_μ both possibilities must be considered. The hyperfine field so obtained is relatively independent of the particular stop site of the muon because of the insensitivity of B_{dip} on the particular site relative to the measurement uncertainties.

In order to determine the sign of B_μ it will be necessary to perform an experiment on a single crystal of Dy and measure the precession sense of the muon when the sample is placed in an external magnetic field.

VII. μSR in α-iron

The transition metal Fe crystallizes in a body-centered cubic structure below 1183 K and is ferromagnetic below $T_C = 1044$ K. The saturation magnetization has been determined at 0 K to be $M_s(0) = 1750$ G and the magnetic moment found to be 2.217 μ_B[44]. The easy axis of magnetization is the $\langle 100 \rangle$ direction. In the bcc lattice there are again two interstitial sites, the octahedral and the tetrahedral sites (see Fig. 23), where the surrounding ions are arranged in a tetragonal symmetry. This implies that in general there are three magnetically inequivalent octahedral sites. With the magnetization along the easy axis the dipolar fields at two of the octahedral sites are equal and have the value −9.3 kG

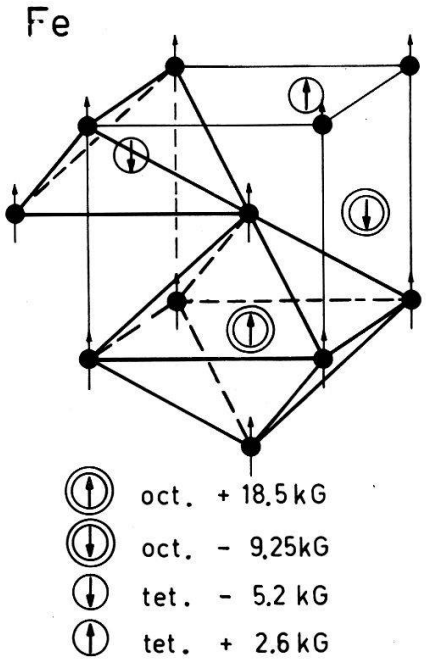

Figure 23
Dipolar fields at the tetrahedral and octahedral interstitial sites in α-Fe at 0 K magnetized along [001]. A muon diffusing rapidly between the octahedral (tetrahedral) sites will average the dipolar fields to zero.

whereas, at the third site $B'_{dip} = +18.5$ kG (see Appendix B). If the muons are stopped at octahedral sites one therefore expects to observe two distinct frequencies in the μSR spectrum. The same argument applies to the tetrahedral sites with different values for B'_{dip}.

The first μSR measurements in Fe performed by Foy et al. [45] and shortly thereafter by Gurevich et al. [46] showed a single muon frequency. It was therefore concluded that the μ^+ diffuses rapidly among the interstitial sites and averages the different dipolar field contributions to zero. It was hoped to be able to observe the localization of the μ^+ at lower temperatures and to obtain information on the diffusion of the muon in iron. These ideas prompted various μSR experiments in Fe [47, 48, 49]. The early measurements at SIN have been published in Ref. 47. Here we report on new data which cover the whole temperature region up to 1000 K.

1. μSR *measurements in* α*-iron*

The results of the observation of B_μ as a function of temperature in the absence of an external field are shown in Fig. 24. In the earliest measurements two single crystal samples were used (□ in Fig. 24). In the high temperature region, above room temperature, a small single crystal ellipsoid was used. Below room temperature the measurements were first made on a 4 cm long single crystal cylindrical sample. Both single crystals were of unknown purity. The signal became very broad and difficult to observe below about 180 K. The later measurements were made on polycrystalline rods of higher purity (99.997%) ((●) in Fig. 24), and the signals could then be observed down to 40 K. A careful search

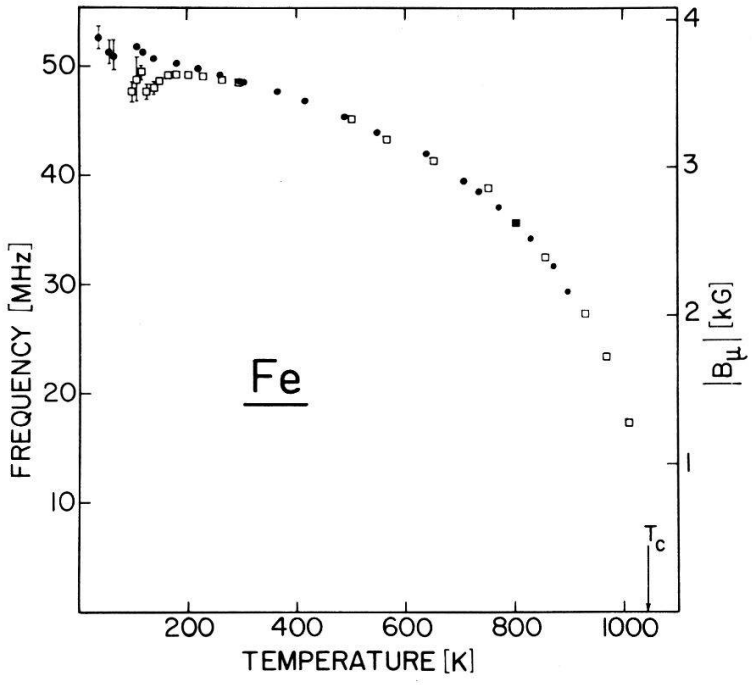

Figure 24
Temperature dependence of the μSR frequency and local field $|B_\mu|$ for Fe in zero external field. Only one frequency is observed over the entire temperature range measured. The (□) represent single crystal measurements and the (●) represent measurements from a high purity (99.997%) polycrystalline rod. Measurements on single crystals showed only a broad signal below 180 K which is probably responsible for the deviation seen below 180 K.

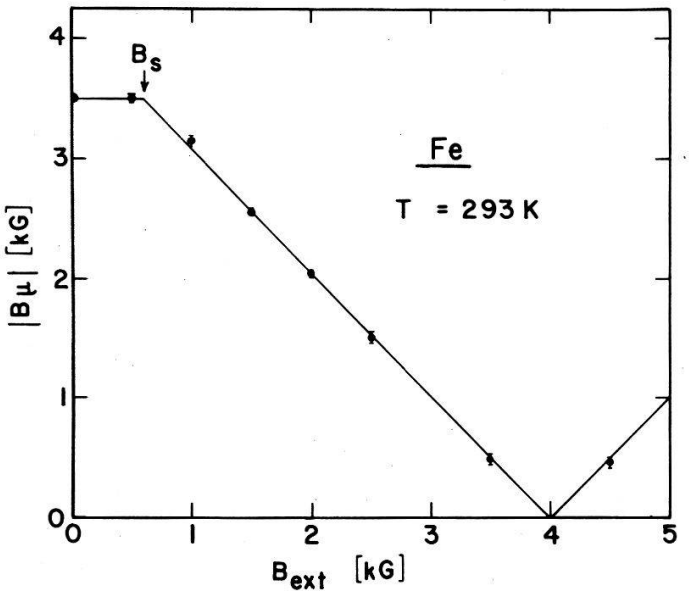

Figure 25
Sign determination at the local field B_μ in Fe. The observation that above saturation (B_s) the μSR frequency decreases with B_{ext} indicates that the internal field B_μ is negative, i.e. opposite to the bulk magnetization.

for the μSR frequency below 40 K revealed no result. Even at 4 K no signals could be detected.

In order to obtain the sign of the local muon field B_μ, measurements were made on the single crystal sample in an external field. The results of these measurements at room temperature are represented in Fig. 25. At an applied field of 590 G the value of B_μ begins to decrease, becoming zero for B_{ext} equal to 4 kG after which the field at the muon increases in absolute value with increasing applied field. These results indicate that the field B_μ at zero applied field must be negatively oriented with respect to the domain magnetization M_s.

The results of the temperature dependence of the depolarization rate for the high purity rods are shown in Fig. 26. For the overlapping temperature range these results are in agreement with earlier measurements on the single crystal [47]. The data show a strong temperature dependence yielding shorter depolarization times as the temperature is lowered until below 100 K the times are shorter than 50 ns.

2. *Interpretation and discussion of results*

The fact that in zero external field only one muon precession frequency is observed indicates that the muons are diffusing rapidly and thus averaging the dipole fields to zero.

With $B'_{dip}=0$ one obtains from equation (8)

$$\vec{B}_\mu = \vec{B}_{ext} - N\vec{M} + \vec{B}_L + \vec{B}_{hf} = \vec{B}_\mu(0) + \vec{B}_{ext} - N\vec{M}, \tag{36}$$

where $\vec{B}_\mu(0)$ is the local field measured in the absence of an external field. Below saturation the last two terms cancel and one is left with $\vec{B}_\mu = \vec{B}_\mu(0)$. With increasing external field the bulk magnetization $\vec{M}$ will increase up to the saturation magnetization $\vec{M}_s$. The field $\vec{B}_\mu$ will change with $\vec{B}_{ext}$ above saturation

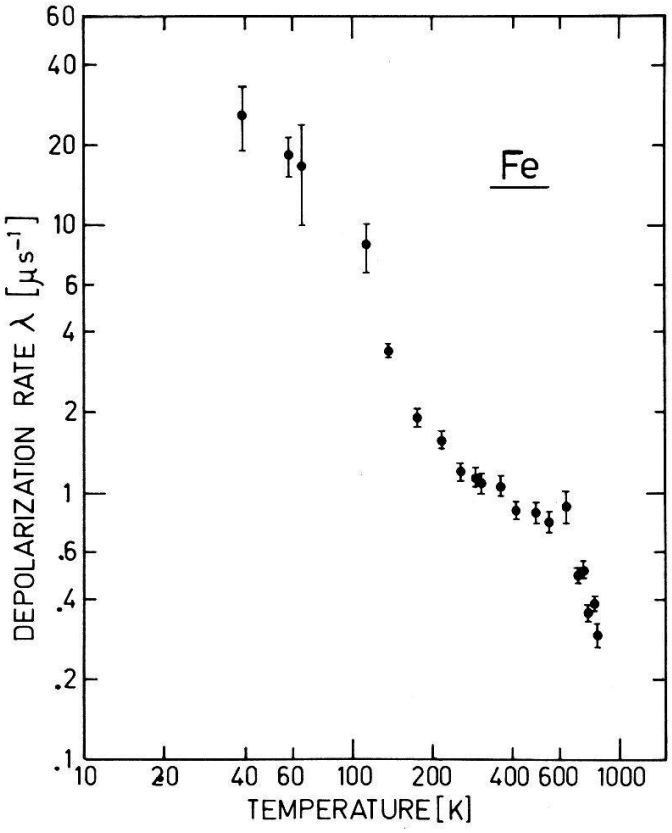

Figure 26
Depolarization rate as a function of temperature for the μSR signal in a high purity (99.997%) polycrystalline iron rod.

according to $\vec{B}_\mu = \vec{B}_\mu(0) + \vec{B}_{ext} - \vec{B}_s$, where $\vec{B}_s = N\vec{M}_s$ is the saturation field. The decrease of $|B_\mu|$ for $B_s < B_{ext} < 4$ kG can only be interpreted by a negative $\vec{B}_\mu$. For values of $B_{ext} > 4$ kG the local field $\vec{B}_\mu$ is parallel to $\vec{B}_{ext}$.

The hyperfine field is obtained as before in the absence of an external field and effective dipole field by subtracting the Lorentz field from the observed B_μ. B_L is determined from $(4\pi/3)M(T)$, where the magnetization $M(T)$ has been corrected for density as a function of temperature [33]. Figure 27 shows the hyperfine field together with the normalized magnetization. The hyperfine field is $B_{hf} = -11.2 \pm 0.2$ kG at $T = 0$ K. The figure illustrates again the characteristic deviation of the hyperfine field from the normalized magnetization as a function of temperature. In this representation B_{hf} in iron falls below the magnetization curve. Possible explanations for this deviation are considered in Section IX.

The observation of a single μSR frequency could be explained by the assumption that the muon becomes trapped at the Fe substitutional sites, which are magnetically equivalent to one another and for which the local dipole field B'_{dip} is zero on symmetry grounds. However, this explanation is excluded on the basis of the strongly temperature-dependent relaxation times and the disappearence of the signal at low temperatures.

The temperature dependence of the depolarization rate is shown in Fig. 26. The overall behaviour is in agreement with other investigations [48, 50]. If the muon diffuses rapidly as indicated by the observation of the single precession frequency then the depolarization can be described in the so-called motional narrowing limit. Under this condition the depolarization can be represented over

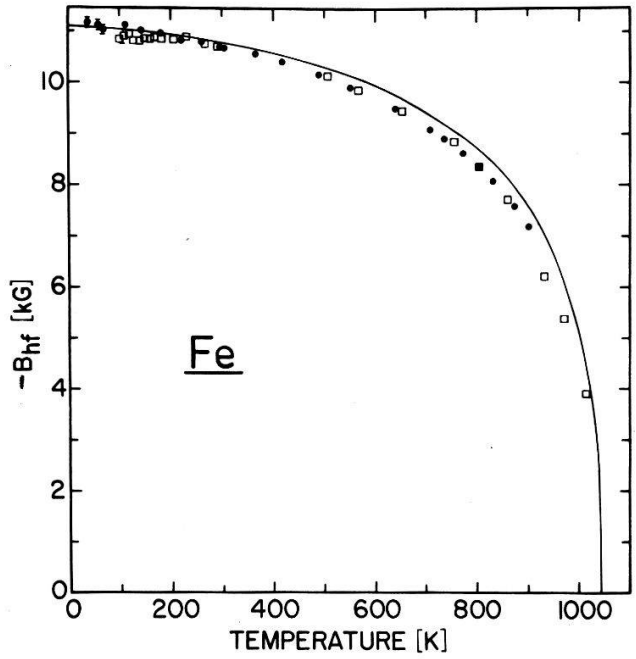

Figure 27
Hyperfine field B_{hf} determined from the μSR data for α-Fe. The single crystal (□) and polycrystalline (●) data fall (except the small deviations discussed in Fig. 25) on the same line which is noticeably below the magnetization curve normalized at 0 K. the hyperfine field at 0 K thus determined is $B_{hf}(0\,\mathrm{K}) = -11.2 \pm 0.2$ kG.

the entire temperature region measured as

$$P(T) = P_0 \exp(-\lambda t), \tag{37}$$

where λ the depolarization rate is given by

$$\lambda = \gamma_\mu^2 B_{dip}'^2 \tau_c \tag{38}$$

with γ_μ being the gyromagnetic ratio of the free muon and where the correlation time τ_c represents the residence time for the diffusing muon. If one is interested in attaining the temperature dependence of τ_c and therefore information about diffusion, it is necessary to normalize to a given B'_{dip}. Since the dipole fields are proportional to magnetization, the $T_2(=\lambda^{-1})$-values must be normalized by the factor $(M(T)/M(0))^2$. Figure 28 shows the temperature dependence of the corrected T_2.

If the assumption is made that the depolarization times are controlled by some activated process, then the Arrhenius plot (Fig. 28) allows the activation energies to be obtained. The fit to the data in Fig. 28 gives for the high temperature region ($T > 650$ K) $E_a = 124 \pm 35$ meV and for the temperature region between 80 K and 350 K the activation energy given is $E_a = 30 \pm 10$ meV. In the lowest temperature region it is difficult to define an activation energy from the three points although it is clear that an effective activation would be quite small.

A determination of an exact mechanism for diffusion at this stage appears difficult and at best speculative. It has been shown [50] the results are quite sample dependent, and the purity and sample preparation seem to be important. Further measurements on well characterized samples are presently being carried out and these results should shed light on the diffusion problem in iron.

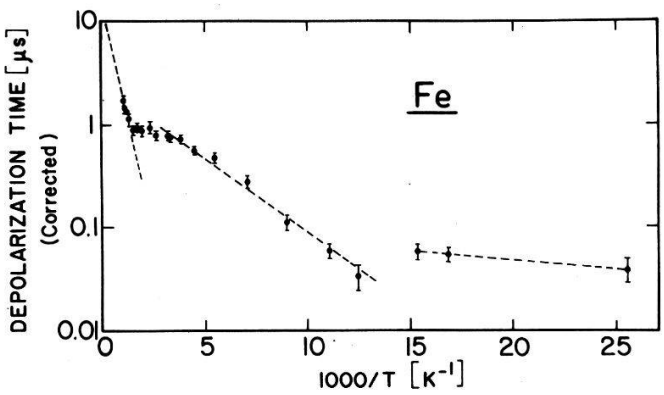

Figure 28
Temperature dependence of the relaxation time T_2 for Fe (corrected depolarization time). In this Arrhenius plot three temperature regions corresponding to different activation energies can be distinguished.

3. *Conclusions*

a) A single muon precession frequency for a given temperature was observed over the entire temperature region measured. The form of this curve as function of temperature roughly follows the magnetization curve.

b) Measurements of B_μ as a function of an externally applied magnetic field have shown the internal field B_μ is negative, or directed antiparallel to the domain magnetization.

c) The hyperfine field at 0 K is $B_{hf} = -11.2 \pm 0.2$ kG. The characteristic deviation from the normalized magnetization curve appears again.

d) Since only one muon frequency is observed over a broad temperature range it is concluded that the muon is diffusing among interstitial sites rapidly enough to average the expected dipolar fields to zero.

e) The relaxation time T_2 shows a strong dependence on temperature, becoming quite short (<50 ns) at low temperatures. There is no complete picture of the mechanisms leading to the depolarization of the muon. It seems clear that the diffusion of the muon is important. Different diffusion mechanisms (trapping, detrapping, tunneling etc.) are probably responsible for the observed behaviour. The fact that different samples show different results indicates that impurities and sample preparation are important.

VIII. μSR in nickel

Nickel, a transition metal, crystallizes in the face-centered cubic structure over the entire temperature range of the solid. The Curie temperature has been measured to be 631.0 K and the magnetic moment to be 0.616 μ_B [44]. The saturation magnetization at 0 K is 528 G. The easy axes of magnetization are along the cubic diagonals. In fcc nickel the octahedral and tetrahedral interstitial sites as well as the Ni substitutional sites (see Fig. 29) have zero local dipole fields due to symmetry.

The first μSR signals in Ni were detected at SREL [45] and further measurements followed at Dubna [46, 51] and Berkeley [52, 53]. More complete

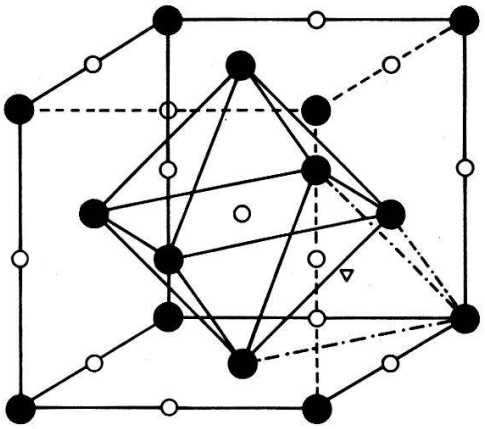

Figure 29
Face centered cubic lattice showing the octahedral (○) and tetrahedral (△) interstitial sites. In contrast to the bcc lattice (Fig. 23) these interstitial sites have cubic symmetry and thus a vanishing dipolar field.

measurements have been made at SIN examining both precession frequency and depolarization time [49] as a function of temperature as well as external field measurements on a single crystal, and these results are reported here.

1. μSR *measurements in nickel*

The results of the temperature dependence of the muon precession frequency in zero field are shown in Fig. 30. The measurements were made on single crystal ((□) in Fig. 30) and polycrystalline samples ((●) in Fig. 30). More than one polycrystalline sample was used which did not appear to affect the muon frequency as the rather continuous behaviour of the results show. Signals could be observed down to 4 K.

For the external field measurements a spherical sample of diameter 2.2 cm was used, which was fabricated to high precision using electroerosion. As in iron,

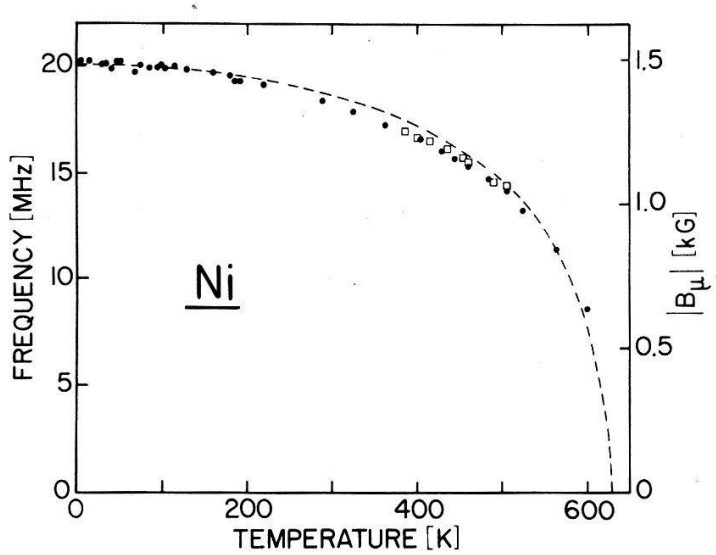

Figure 30
Temperature dependence of the μSR frequency for single crystal (□) and polycrystalline (●) Ni. The right-hand scale gives the absolute value of the local field B_μ.

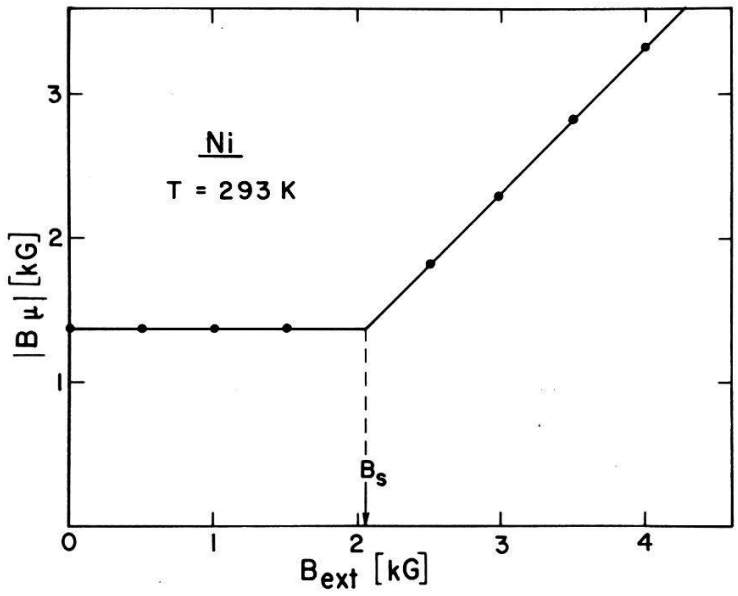

Figure 31
Local field $|B_\mu|$ as a function of external field B_{ext} for a single crystal Ni sphere. At the saturation $B_s = (4\pi/3)M_s$ the μSR frequency starts to increase with B_{ext}, thus indicating that the internal field B_μ is positive, i.e. in the direction of the bulk magnetization.

the behaviour of the local field B_μ with the application of an external field yields information as to the sign of the local field with respect to the domain magnetization. The results of these measurements are shown in Fig. 31. Clearly, B_μ increases as the external field becomes larger than the saturation field, B_s. The value of B_s determined from the function of the linear extrapolation of the high and low external field regions is 2050 ± 13 G.

Figure 32 shows the measured depolarization time, T_2, as a function of temperature. The measurements were made on high purity polycrystalline foils. In the range 4 K to 300 K the depolarization times are temperature-independent

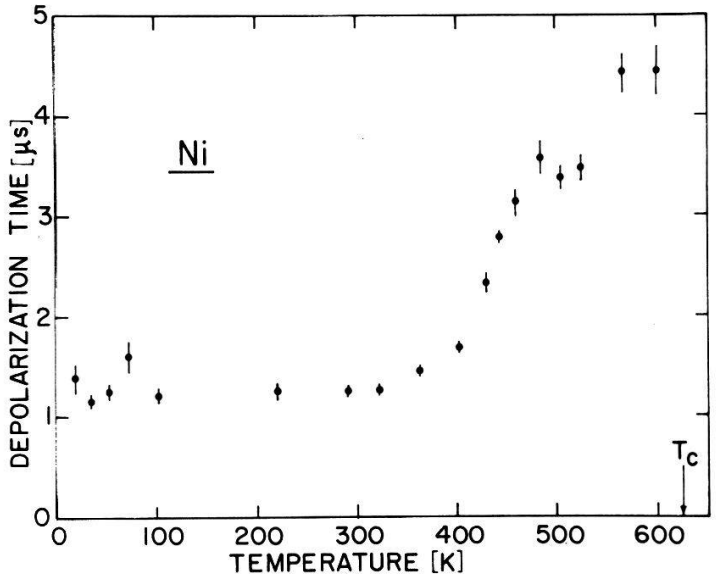

Figure 32
Temperature dependence of the depolarization time of the μSR signal in high purity polycrystalline Ni foils.

with a value near 1 μs. As the temperature is raised from 300 K to 550 K the relaxation time increases reaching 4.6 μs at 550 K. Above 550 K the depolarization rate appears constant.

2. *Interpretation and discussion of* μSR *in* Ni

The hyperfine field as a function of temperature (Fig. 33) has been calculated from the zero field data shown in Fig. 30 as

$$\vec{B}_{\mathrm{hf}} = \vec{B}_{\mu} - \frac{4\pi}{3}\vec{M}_{\mathrm{s}}, \tag{39}$$

where the saturation magnetization was again corrected for density [33]. The hyperfine field thus obtained at 0 K is $B_{\mathrm{hf}}(0) = -0.707 \pm 0.010$ kG.

In Fig. 33 the hyperfine field $B_{\mathrm{hf}}(T)$ is compared with the normalized magnetization curve ($(M_{\mathrm{s}}(T)$). The figure indicates again that the hyperfine field is not proportional to the magnetization. It should be noted in the case of Ni the deviation of the hyperfine field, in contrast to the other ferromagnetic materials studied, is in the positive direction from the normalized magnetization.

The fact that the measured B_{μ} is increased when an external field greater than the saturation value, B_{s}, is applied, shows that the internal field B_{μ} and the domain magnetization M_{s} have the same direction. The B_{S}- value obtained, 2050 ± 13 G, is in excellent agreement with expected for an ideal spherical sample ($(4\pi/3)M_{\mathrm{s}}(293\ \mathrm{K}) = 2048$ G).

The temperature dependence of T_2 (Fig. 32) can be divided into two regions. In the low temperature region, $T < 300$ K, the measurements give a depolarization time of 1.0 μs. A radiation damage study [55] indicated that the absolute value of this depolarization time could be shortened by a factor of three.

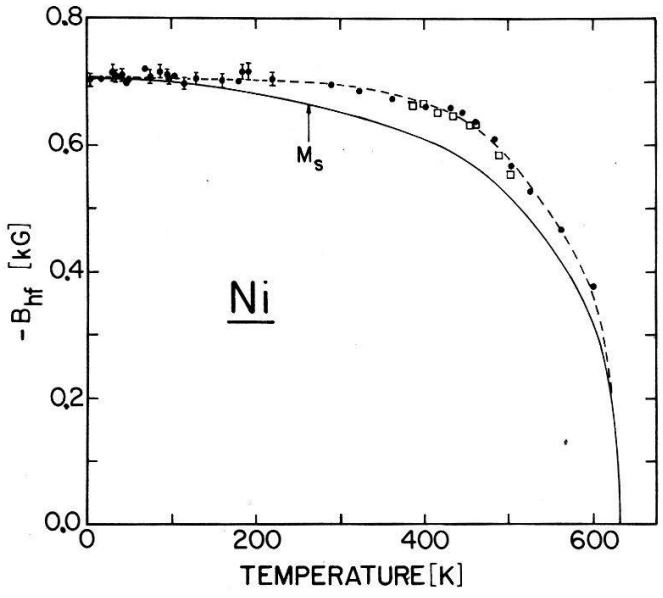

Figure 33
Hyperfine field determined from μSR data in Ni. The hyperfine field at 0 K is $B_{\mathrm{hf}} = -0.707 \pm 0.010$ kG. The bulk magnetization curve $M_{\mathrm{s}}(T)$ normalized at 0 K is definitely below B_{hf} in this representation.

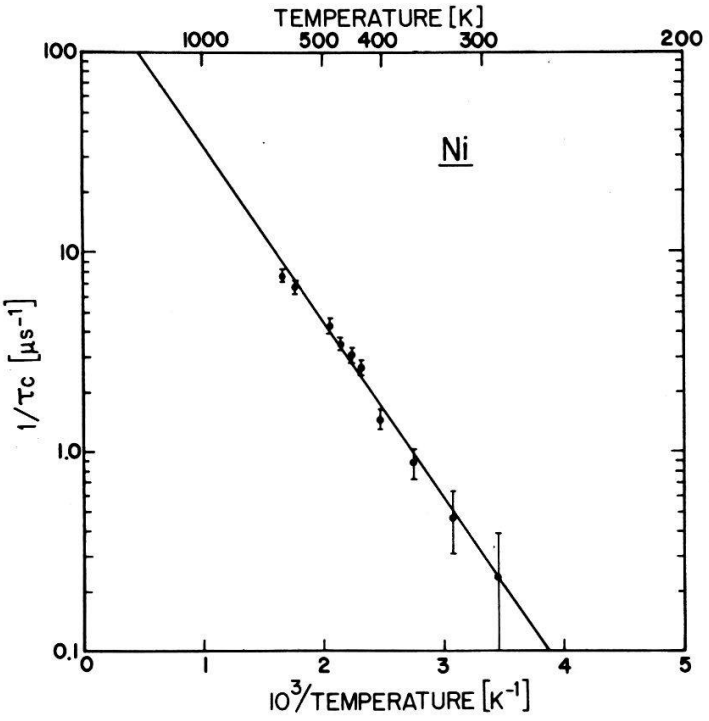

Figure 34
Temperature dependence of the inverse correlation time in Ni. The straight line is a fit to the Arrhenius law.

The observed T_2's are probably resulting from inhomogeneous broadening in the sample over this temperature range. In the high temperature range, $T > 350$ K, the value of the depolarization time is most probably determined by motional narrowing. In Ni the electronic dipole fields from the normal interstitial and substitutional sites are zero so the perturbing fields producing relaxation have their origin in impurities or defects. If a fit is made to the relaxation function [56]

$$P(t) = P_0 \exp\{-2\sigma^2\tau_c^2(\exp(-t/\tau_c) + t/\tau_c - 1)\} \tag{40}$$

over the temperature range $350\text{ K} < T < 550\text{ K}$, and the assumption is made that σ is constant and the correlation time τ_c is governed by an activated process ($\tau_c = \tau_\infty e^{-(E_a/kT)}$), then one obtains with $\sigma = 0.81\ \mu\text{s}^{-1}$ the correlation time as a function of temperature as shown in Fig. 34. The temperature dependence of τ_c is given with an activation energy of 173 ± 7 meV with the pre-exponential factor $\tau_\infty = 10^{-(8.4\pm0.05)}$s [54].

3. *Conclusions*

a) The temperature-dependent behaviour of the muon precession data generally exhibits the magnetization behaviour. At $T = 0$ K, B_μ is 1.5 kG and for higher temperatures the value of B_μ gradually decreases until at the Curie point (631 K) the field is zero.

b) The application of an external field of strength greater than that of the saturation field showed an increase in B_μ indicating the local field and the magnetization are in the same direction. The value of B_s, the saturation field, is equal to that expected for the spherical sample.

c) At $T=0$ K the hyperfine field is negative with a value -0.707 ± 0.010 kG. A comparison of B_{hf} with the normalized magnetization shows a positive deviation of the hyperfine field from the magnetization. This result is opposite to that obtained for all the other ferromagnetic metals measured.

d) The observed temperature dependence of T_2 may be explained by the motional narrowing phenomenon. The activation energy in the intermediate temperature range is $E_a=173\pm7$ meV.

IX. Hyperfine fields

In the previous sections it has been shown how it is possible to analyze the various contributions to the measured local field B_μ. This section is devoted to a discussion of the hyperfine field B_{hf}. The resulting values for B_{hf} are first compared to the information obtained from neutron scattering data (IX.1). Then various theoretical models for B_{hf} are critically examined (IX.2) and the observed temperature dependencies $B_{hf}(T)$ are discussed (IX.3).

Based on the interpretation of the μSR data in the various ferromagnets which lead to the conclusions that the muon is sitting at the octahedral site in Co and Gd, and that the residual dipolar field B'_{dip} vanishes in Ni and Fe, the following values are obtained for the hyperfine fields extrapolated to $T=0$ K:

Fe	-11.1 ± 0.2 kG
Co	-6.1 ± 0.2 kG
Ni	-0.71 ± 0.01 kG
Gd	-6.9 ± 0.2 kG
Dy	-0.7 or -25.2 ± 1.0 kG,

where the two values for Dy correspond to the two possible signs for B_μ.

The obvious common feature of these values is their negative sign which means that the magnetization densities at the muon are in opposite direction to the averaged magnetization densities in the unit cell. Such a negative value is in agreement with other experiments at dilute non-magnetic impurities in ferromagnetic metals which generally show negative hyperfine fields for small valence Z of the impurity and positive ones for high Z. This feature was explained by the Daniel–Friedel model [57]. Before outlining this model the information on the magnetization density as obtained from neutron scattering data is discussed.

1. *Information from neutron scattering data*

Via the magnetic interaction, neutrons probe the magnetization $\vec{M}$ in ferromagnetic crystals. The magnetic interaction is given by $-\vec{\mu}_N\cdot\vec{B}(\vec{r}_N)$, where the $\vec{\mu}_N$ is the magnetic moment operator and $\vec{B}$ the field at the neutron site $\vec{r}_N$. Whereas the magnetization $\vec{M}(\vec{r})$ in the magnetic unit cell is expected to exhibit a simple space dependence, the variation of $\vec{B}(\vec{r})$ may be quite complicated. The Fourier transform of $\vec{B}(\vec{r})$, however, can easily be expressed in terms of $\vec{M}$

$$\vec{B}(\vec{k})=4\pi(\vec{M}(\vec{k})-\hat{k}(\hat{k}\cdot\vec{M}(\vec{k})) \tag{41}$$

since $\vec{k}\cdot\vec{B}(\vec{k})=0$ and $\vec{k}\times\vec{H}(\vec{k})=0$.

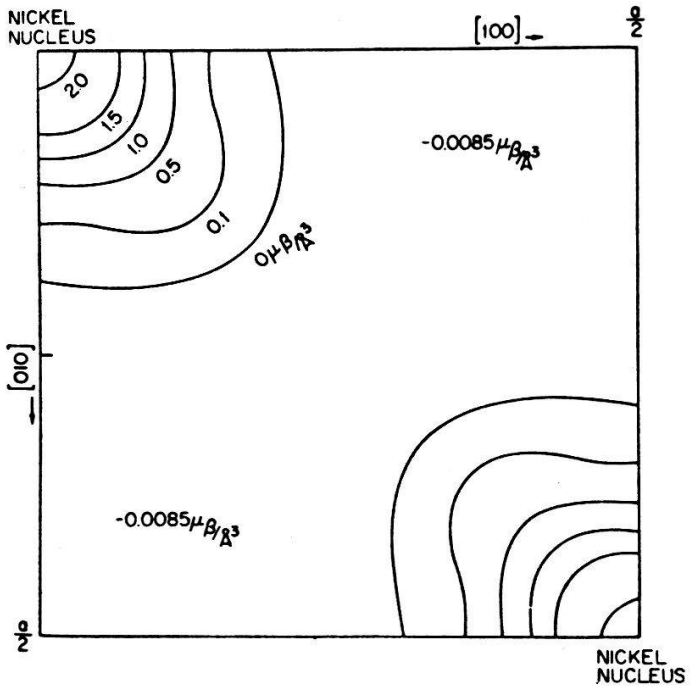

Figure 35
Magnetic moment distribution in the (100) plane in Ni obtained from polarized neutron Bragg scattering (Ref. 59).

Using polarized neutron beams the magnetic scattering amplitude has been determined by Bragg scattering in ferromagnetic Fe [58], Ni [59], Co [14], and Gd [25]. The results for the transition metals have been reviewed by Shull [60]. The magnetization distribution can be determined as a Fourier series expansion of the magnetic Bragg reflection amplitudes. In Fig. 35 the results [59] are shown for the (111) plane in Ni and in Fig. 36 for Fe [60]. The Fourier series give accurate

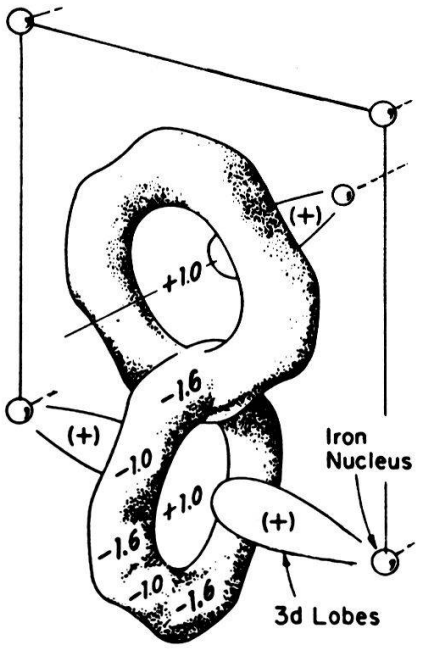

Figure 36
Model of the magnetization distribution in the bcc unit cell of Fe (Ref. 60). The very large positive magnetization around the atoms is not shown.

results for the distribution in the region near the lattice sites, but converges too slowly to give information in the interstitial region since only a finite number (about 30) of Bragg reflections could be measured. By averaging the magnetization over regions of space, the effects due to finite resolution were minimized. In Ni the resulting value of the magnetization in the interstitial region is $M_0 = -0.0085\ \mu_B/\text{Å}^3$. For Fe the values are $M_0 = +0.0085 \pm 0.0068\ \mu_B/\text{Å}^3$ for the octahedral site and $M_0 = -0.0136 \pm 0.0043\ \mu_B/\text{Å}^3$ at the tetrahedral site [61]. At the octahedral site hcp Co one obtains $M_0 = -0.020\ \mu_B/\text{Å}^3$. An alternative way of analyzing the neutron scattering data is to fit the measured magnetic form factor to a free-atom 3d spin form factor and a constant term. This constant term corresponds to a uniform contribution of the magnetization with values $-0.018\ \mu_B/\text{Å}^3$ for Fe [58], $-0.0092\ \mu_B/\text{Å}^3$ for Ni [59] and $-0.025 \pm 0.006\ \mu_B/\text{Å}^3$ for Co [14].

The qualitative result from all the neutron scattering data is the indication that a distribution $M_l(\vec{r} - \vec{R}_{\vec{n}})$ of positive magnetization is localized around each atom superimposed on a constant negative background M_0. The localized distribution is nearly spherically symmetric for Co, and shows asymmetries along the [110] direction in Ni and along the [100] directions in Fe. This picture helps to clarify the origin of the various contributions to the local field B_μ at a muon, which have been discussed in Section III. If the charge of the muon would not change the electronic environment the constant term M_0 would give rise to a contact field

$$B_{\text{hf}} = \frac{8\pi}{3} M_0 \tag{42}$$

which is sometimes referred to as the ambient hyperfine field. The interaction with the localized moments can be described by the dipolar interaction with moments $\vec{\mu}(\vec{m})$ localized at the lattice sites $\vec{m}$, and where the Lorentz field is given by the average of $(4\pi/3)(M_l + M_0)$ which is proportional to the saturation magnetization M_s.

The screening of the muon charge leads to an appreciable distortion of the local electronic structure. Whereas, in simple metals the screening can be expected to arise from a rearrangement of s-like conduction electron states, in transition metals an additional contribution may arise from a distortion of the d-wave functions. It is also conceivable that the presence of the μ^+ then even changes the magnetic properties of the neighbouring ions. A microscopic theory accounting for these effects is difficult. Some first steps in that direction have been made [62, 63, 64] without, however, covering all aspects. It has to be mentioned that already in the undisturbed case a microscopic theory meets great difficulties. Although band structure calculations give results which are in good agreement with the measurements for the magnetization distribution around the ions, they are very uncertain in prediction for the interstitial region. As an example we refer to Harmon and Freeman [65] who indicate a value of $-0.002\ \mu_B/\text{Å}^3$ for the magnetization at the octahedral site in Gd, where the small value of M_0 is obtained as the difference between 0.043 for the spin-up and 0.045 for the spin-down density. This has to be compared to the experimental value of $-0.037\ \mu_B/\text{Å}^3$. Accounting for the additional presence of an impurity makes a first-principle calculation a formidable task. Any theory which aims at an ab initio

determination of the hyperfine field has first to be tested in the undisturbed case, where it is not only sufficient that good eigenvalues and energy bands are reproduced but also that eigenfunctions are obtained. These wave functions are, however, much more sensitive to approximations. Therefore we concentrate in the following on simplified models where the influence of different physical mechanisms on spin densities at impurities can be investigated.

2. *Model calculations for* B_{hf}

The best known model for hyperfine fields at dilute nonmagnetic impurities in ferromagnetic metals is that of Daniel and Friedel [57] who assume a homogeneous free electron gas with a positive spin polarization. Simulating the electrostatic potential of the impurity by a square-well potential whose depth depends on the impurity valence charge Z, the spin densities at the impurity are calculated. Negative hyperfine fields result for small Z and positive ones for high Z. Although most applications of this model have dealt with substitutional impurities, it is equally well applicable to interstitial impurities. Another model for hyperfine fields was proposed by Blandin and Campbell [66] who, instead of assuming an *a-priori* spin polarized electron gas, considered explicitly the interaction between the localized moments of the host and the conduction electrons giving rise to an inhomogeneous spin polarization. Recently, a generalized model has been developed [67] which contains both the models of Daniel and Friedel and of Blandin and Campbell as limiting cases. The model has been applied [68] to a calculation of the hyperfine fields at muons in Gd and Dy.

Previous calculations [69] of the spin density at muons in ferromagnetic metals started from an electron gas with a homogeneous band splitting determined from the background magnetization density M_0 measured with neutron scattering. The charge screening of the muon then leads to an enhanced magnetization M which has the same sign as M_0. As has been pointed out [68] such a treatment is inadequate since the background density M_0 cannot be attributed to a homogeneous conduction electron polarization. This is evident in the case of Gd where the mean conduction electron spin density is positive ($+0.55\ \mu_B$/atom) while M_0 is negative.

The model developed in Ref. 67 starts from free conduction electrons which interact with the moments $\vec{S}$ localized at the lattice sites $\vec{m}$ through an effective $s-d$ or $s-f$ exchange interaction

$$H_{\mathrm{ex}} = -2J\Omega\vec{s}\cdot\vec{S}\delta(\vec{r}-\vec{R}_{\vec{m}}) \tag{43}$$

with interaction energy J and where Ω denotes the atomic volume. This interaction is simulated by a spin dependent potential

$$W_\sigma(\vec{r}) = -\sigma J\Omega\langle S_z\rangle\sum_{\vec{m}}\delta(\vec{r}-\vec{R}_{\vec{m}}) \tag{44}$$

where $\sigma = \pm 1$ according to the spin projection of the conduction electrons. The average value of W_σ is given by

$$\bar{W}_\sigma = -\sigma J\langle S_z\rangle. \tag{45}$$

This gives rise to a homogeneous spin density

$$\Delta n_0 = J\langle S_z\rangle z(E_F) \tag{46}$$

with $z(E_F)$ denoting the density of states at the Fermi energy. To fix the exchange interaction it is assumed that Δn_0 accounts for the excess moment of the magnetization which is 0.55 (0.2) μ_B for Gd (Dy). The model then gives an unperturbed hyperfine field (ambient field) $B_{hf}^0 = -0.96$ kG at the octahedral interstitial site in Gd, and $B_{hf}^0 = -0.68$ kG for Dy. Thus for both metals the positive average conduction electron magnetization is locally reversed to a negative value. The reason for this is the oscillatory behaviour of the spin densities induced by the interaction (44) as is well known from the RKKY theory.

Introducing now a muon at $r = 0$ with a screened electrostatic potential $V(r)$ we have the total potential $V(r) + W_\sigma(r)$, where

$$W_\sigma(r) = \int \frac{d\Omega}{4\pi} W_\sigma(\vec{r}). \tag{47}$$

This averaging over angles allows the application of potential scattering theory in a simple way. It is convenient to split up the total potential into a contribution

$$V_0^\sigma(r) = V(r) + \theta(r - R_0)\bar{W}_\sigma, \tag{48}$$

which consists of the screened electrostatic potential of the muon with range R_0 and the averaged exchange potential of the magnetic ions and into a contribution

$$\phi^\sigma(r) = -\sigma J\langle S_z\rangle\left(\Omega \sum_s \frac{Z_s}{4\pi R_s^2}\,\delta(r - R_s) - \theta(r - R_0)\right), \tag{49}$$

where the sum extends over all shells s of radius R_s from the μ^+ and where Z_s denotes the number of ions on shell s. $\phi^\sigma(r)$ vanishes for $r < R_0$ and falls to zero as r becomes large. The potential V_0^σ is treated without approximation by calculating the phase shifts $\delta_0^\sigma(k)$ and the enhancement factor $E_0^\sigma(k)$ which gives the density of the wave-functions at the origin. The influence of $\phi^\sigma(r)$ is then taken into account in the distorted wave Born approximation with the result [67]

$$E^\sigma(k) = E_0^\sigma(k) \exp\left\{-\frac{2}{k}\int_0^\infty dr \Phi^\sigma(r) \sin(2kr + 2\delta_0^\sigma(k))\right\}. \tag{50}$$

The contribution of the scattering states to the spin density at the origin is then given by

$$\Delta n(0) = \frac{1}{V}\sum_{k<k_F^+} E^+(k) - \frac{1}{V}\sum_{k<k_F^-} E^-(k). \tag{51}$$

The results [68] of the model for the hyperfine fields at the muon are summarized in Table III. The screening potential $V(r)$ has been approximated by a

Table III
Calculated hyperfine fields at the muon

	Gd	Dy
octahedral site	−2.7 kG	−1.5 kG
tetrahedral site	−3.9 kG	−2.5 kG

square-well potential to allow the use of the DWBA. The values are obtained by summing over 40 shells, the nearest-neighbour shell contributes typically 70% of the total value. The unperturbed values are enhanced by a factor of 2−3 which is considerably less than the enhancements obtained in those model calculations [69] which started from a homogeneous electron spin-density. In addition to the distortions due to the muon charge, in the present case one also has distortions due to the inhomogeneous potential [44] which clearly show up in the negative hyperfine fields in the undisturbed case.

The model has not yet been applied to a calculation of the muon hyperfine field in transition metals where the assumption of a localized exchange interaction between local moments and conduction electrons is much more questionable than in the rare-earth metals. A nice feature of the model, however, is that is predicts the change in the hyperfine field upon a change in the magnetic structure, which is of relevance for Dy as has been pointed out in Section VI.

The change from the ferromagnetic to the helical spin arrangement can be accounted for by an appropriate decomposition of the contributions of the spin moments of shells in equation (8). The resulting change of B_{hf} in Dy has been calculated as a function of the turn angle α of the helix (see Fig. 37). Changing α from 0° to 26° gives only a reduction of 3% in B_{hf}. The small size of this effect is partly due to the overwhelming contribution of the first neighbour shells and partly due to the compensation of the positive and negative contributions of outer shells. This gives an explanation for the observation that measured local fields B_μ in Dy did not change appreciably at the phase transition from the ferro- to the antiferromagnetic state. The limited accuracy of the data, however, does not allow to draw further conclusions. More detailed experiments on Dy would be of great help.

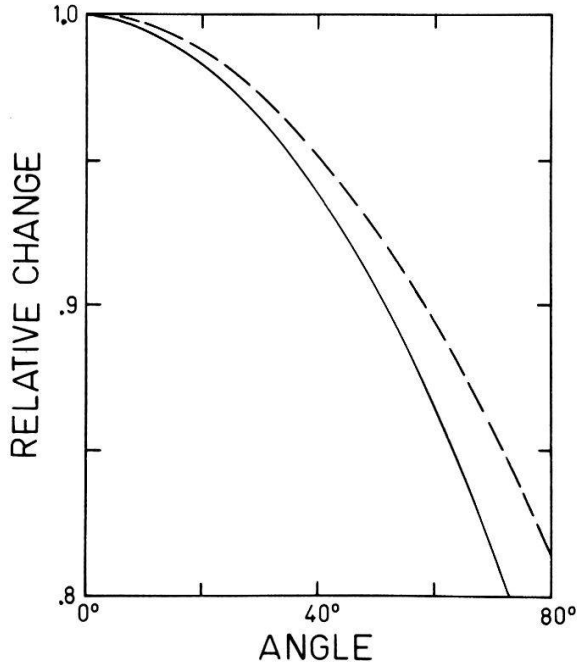

Figure 37
Relative change of the hyperfine fields in Dy as a function of the helix turn angle. Ths solid line refers to the octahedral interstitial site, the dashed line to the tetrahedral site.

3. *Temperature-dependence of* B_{hf}

In the Sections IV–VIII, where the μSR experiments in the various ferromagnetic metals have been analyzed, it has been shown that the temperature-dependence of the extracted hyperfine field $B_{hf}(T)$ follows, on the whole, the temperature-dependent saturation magnetization $M_s(T)$. There are, however systematic deviations in the temperature-dependence which will now be discussed. As with the negative sign of the hyperfine field this feature is again not particular to the muon impurity, but is observed quite generally at various dilute non-magnetic impurities in ferromagnetic metals. As an example we refer to recent measurements [70] of $B_{hf}(T)$ at Ga, Ge, and As impurities in Co by perturbed angular correlation techniques.

Both the Daniel–Friedel [57] and Blandin–Campbell [66] models lead to a proportionality between B_{hf} and M_s. The theory discussed in IX.2, however, exhibits a non-linear dependence of the hyperfine field on the host magnetization. In the framework of this model it is assumed that the temperature-dependence of the localized moment $\langle S_z \rangle$ is given by that of $M_s(T)$:

$$\langle S_z(T) \rangle = \langle S_z(T=0) \rangle M_s(T)/M_s(0). \tag{52}$$

An inspection of the expression for the enhancement factor, equation (50), shows that the temperature-dependent exchange potential Φ^σ occurs in the exponential. The spin density at the muon then is proportional to $M_s(T)$ only if it is allowed to linearize expression (50). This is the case close to the Curie temperature. In general, however, the temperature dependence of $\Delta n(0)$ does not scale with $M_s(T)$. This has been calculated [67] for Gd with the result shown in Fig. 38. The theoretical result agrees qualitatively with the experiment (see Fig. 19). In view of the assumptions of a free electron gas, these results seem satisfactory.

A discussion of the temperature dependence also has to include an investigation of the influence of lattice vibrations. The analysis of the various contributions to the local field B_μ in Section III was based on a calculation of the residual dipolar field B'_{dip} arising from local moments $\vec{\mu}$ at rigid lattice sites. While the thermal expansion of the lattice was accounted for, the oscillations of the ions and

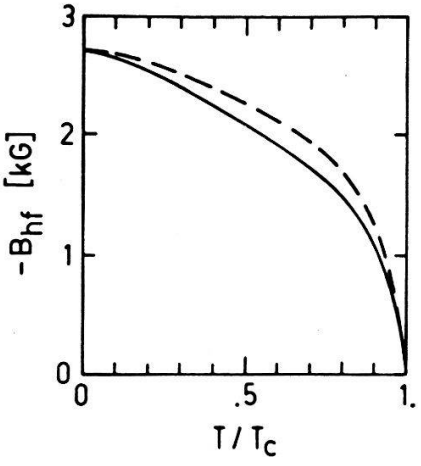

Figure 38
Temperature dependence of the calculated hyperfine field for a positive muon at an octahedral interstitial site in gadolinium. The dashed line is the host magnetization normalized to $B_{hf}(T=0\,\mathrm{K}) = -2.75$ kG. This figure should be compared with Fig. 19.

of the muon around their equilibrium sites have been neglected. A justification has been given in Ref. 7 based on the fact that the value of B'_{dip} averaged over a spherically symmetric probability distribution of the muon or the ions coincides exactly with the value for pointlike magnetic moments. The transferred hyperfine field B_{hf}, however, may be influenced by the lattice vibrations [71]. In the framework of the model discussed in IX.2 the interaction (43) actually depends on the instantaneous positions of the ions. Since the muon precession frequency is very low compared to phonon frequencies one has to average the interaction potential W_σ over the phonon fluctuations. This gives rise to a reduction of the spin-dependent potential by a Debye-Waller factor and may be responsible for the peculiar temperature-dependence of B_{hf}.

X. Summary

It is of interest to review the μSR results in this set of ferromagnetic metals i.e. the transition metals Fe, Co, Ni and the rare earth Gd and Dy. It appears through the systematic study of these materials that a consistent picture of the major interactions with muons on the atomic scale exists. At the same time, various questions such as the mobility of the muon and the manner in which it influences its own environment are left still unanswered.

In all of these metals the muon remains as a bare particle without binding to an electron. As such the muon probes the internal fields. As has been shown both the sign and magnitude of the local field, B_μ, can be obtained. The sign, which gives the direction of the local field with respect to the domain magnetization, has been determined in the case of Fe and Ni by observing the muon precession frequency when an external field is applied above the saturation value, and in the case of Co by observing the precession sense of the muon. The local field B_μ is given by

$$\vec{B}_\mu = \vec{B}_{\mathrm{ext}} + \vec{B}_{\mathrm{dem}} + \vec{B}_{\mathrm{L}} + \vec{B}'_{\mathrm{dip}} + \vec{B}_{\mathrm{hf}}, \tag{8}$$

where the various contributions have been defined in the main text. The contribution, B_{hf}, the hyperfine field, arises from the spin polarization of the conduction electrons and represents the quantity of main physical importance. Table IV summarizes the results from the measurements showing the relative strength of the various contributions to the magnetic field at the site of the muon.

The existence of the dipole fields and the ability to calculate this contribution to the local field have been shown to be important. For the case of Gd and Co an understanding of the origin of the dipole field and its dependence on local spin direction allowed the unique determination of the muon stop site. Further the calculation of the total dipole field in Dy was in good agreement with observation over both ferromagnetic and antiferromagnetic phases. The fact that the measured local field does not change discontinuously across the magnetic phase transition is in agreement with the calculated dipole fields. It is noteworthy that the data may be explained using the dipole calculations under the assumptions of localized dipole moments.

The role of diffusion of the muon has been shown to affect drastically the measured local fields. As extreme cases one may compare the results in Fe with

Table IV
Compilation of some properties of the ferromagnetic metals investigated and summary of the μSR results. All data are extrapolated to $T = 0$ K.

Substance	Structure	Saturation magnetization M_s [kG]	Local field at Muon B_μ [kG]	Hyperfine field B_{hf} [kG]	Calculated dipolar field B'_{dip} [kG] octah.		tetrah.	Muon site
Fe	bcc	1.750	− 3.67 ±0.10	−11.1 ±0.2	− 9.26 +18.52	a)	+2.63 −5.25	?
Co	hcp	1.415	− 0.317±0.010	− 6.1 ±0.2	− 0.242		+0.199	octahedral
Ni	fcc	0.528	+ 1.48 ±0.10	− 0.71±0.01	0		0	?
Gd	hcp	2.010	+ 1.10 ±0.05	− 6.98±0.10	0.658		0.020	octahedral
Dy	hcp	2.995	±12.30 ±0.20	−25.2 or − 0.7 ±1.0	0.487		0.430	?

a) For the dipolar field values in Fe see the discussion in Appendix B and Fig. 23.

those for Dy. In the case of iron the motion of the muon averages out the different dipole fields expected for a stationary muon. In contrast, the fact that a muon precession signal is observed in antiferromagnetic Dy can only be explained if the muon remains localized at a given site. It has been shown particularly for Fe and Ni that the purity and preparation of a sample influences diffusion. At the present time it is not possible to predict the diffusion behaviour of a muon in a given substance. Various theories and models exist which attempt to explain the observations but, a true understanding of the mechanisms by which a muon moves in a material together with the temperature dependence still remains one of the major unanswered questions in μSR work.

The measurement and interpretation of the hyperfine field, B_{hf}, is particularly important because of the possibility of measuring interstitial magnetization. Magnetic metals are of special value when considering this question since the origin of the field is the magnetism of the conduction electrons. The muon as an impurity, however, modifies the charge and spin density in its own neighbourhood. A prerequisite to the extraction of the natural interstitial magnetization is an understanding of the spin enhancement factor due to the muon itself. Theoretical models have been proposed to account for this perturbations and while the picture is clearing somewhat, this remains one of the problems to be solved. Nonetheless, a knowledge of the origin of B_{hf} at the muon site is at the core of understanding the interaction of the muon with its environment and as such should encourage further experiments and theoretical studies.

In summary, it appears that the muon can be used to probe the magnetic environment on the atomic scale and therefore can be used as a tool to study electron spin densities and magnetic ordering phenomena. In the last three or four years good progress was made in understanding muons in ferromagnets, and now the muon may be used as a microscopic probe in the study of magnetization.

Acknowledgment

The authors wish to thank Dr. B. D. Patterson for his contributions in helping to get our μSR program started and for his participation in many of the measurements; Dr. W. Reichart for his constant help with the data acquisition system, and K. Rüegg for various contributions to the dysprosium work. The authors are grateful to Prof. J. P. Blaser, director of SIN for his support and interest in the μSR program, and to the staff of SIN and our Physics Institute for technical support.

Appendix A

In order to increase the statistical accuracy of the measurements it is advantageous to eliminate the low energy positrons. By doing this the counting rate will decrease but the desired asymmetry will increase. A best situation exists whereby the maximum information may be obtained in the shortest time.

The distribution of positrons decaying into a given solid angle as a function of energy ($\varepsilon = E/E_{max}$) is given in equation (1). Integrating this equation from a

lower cutoff ε_c to the maximum energy $\varepsilon = 1$, the asymmetry is given as

$$A(\varepsilon_c) = (1 + 2\varepsilon_c^3 - 3\varepsilon_c^4)/3 - 6\varepsilon_c^3 + 3\varepsilon_c^4), \tag{A1}$$

which is shown in Fig. 1.

For the measurement it is the statistical accuracy of the asymmetry parameter which is important. The statistical error of the asymmetry given as a function of the cutoff energy is

$$\frac{\Delta A}{A}(\varepsilon_c) = [(1 - 2\varepsilon_c^3 + \varepsilon_c^4)/(N\Omega/8\pi)]^{1/2}/(\tfrac{1}{3} + \tfrac{2}{3}\varepsilon_c^3 - \varepsilon_c^4), \tag{A2}$$

where N is the number of muon stops in the target and $\Omega/4\pi$ the solid angle of the positron detector. This function shows a flat minimum at a cut-off energy of $\varepsilon_c = 0.735$. An absorber for positrons with energy below ε_c would allow to decrease $\Delta A/A$ for a given counting time by 23%, compared to a measurement without the absorber. Or, the time required to get the same accuracy using an absorber will decrease by 41%.

In the actual μSR experiment the target size, the relaxation-time T_2 and the effective asymmetry all have to be considered. The spectrum is usually described by

$$Y = c(1 + A_{\text{eff}} \exp(-t/T_2) \cos \omega t) \exp(-t/\tau_\mu). \tag{A3}$$

For practical purposes the time $t_{10\%}$ to determine an asymmetry with relative error of $\Delta A/A = 0.1$ was calculated as a function of the absorber and target thickness. The error calculation applied to equation (A3) gives

$$t_{10\%} = F(T, D)(1 + 2\tau_\mu/T_2) \Big/ \left\{ \text{nm} \frac{\Omega}{4\pi} r^2 [1 - \exp(-t/\tau_\mu - 2t/T_2)] \right\}. \tag{A4}$$

The function $F(T, D)$ is plotted in Fig. 39 for $T = 1$, 4, 7, and 10 g/cm^2 target

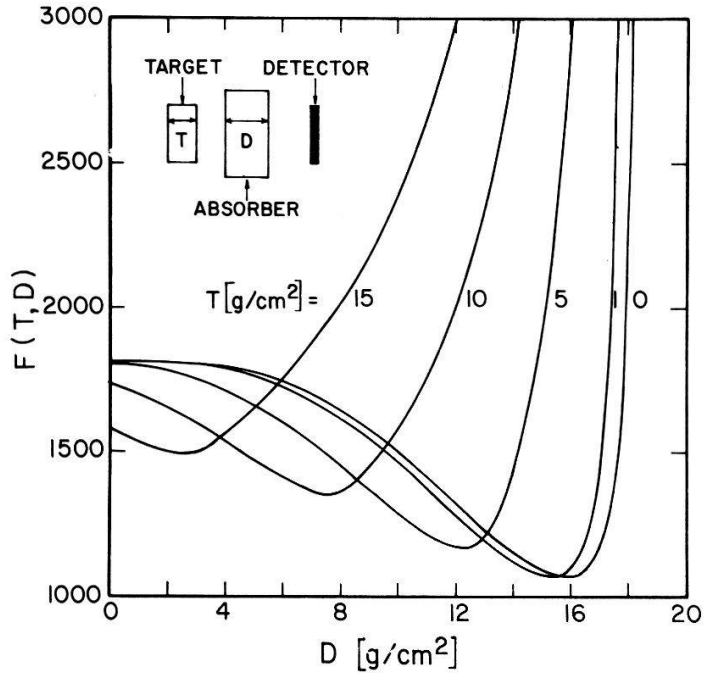

Figure 39
The function $F(T, D)$ used to estimate an optimal positron absorber thickness D in order to decrease the measuring time in a μSR experiment. T is the target thickness.

thickness as a function of the absorber thickness D. n is the muon stop rate per gram, m the target mass, $(\Omega/4\pi)$ the β^+-detector solid angle, $r = A_{\text{eff}}/A_{\text{calc}}$ is the reduction factor for the asymmetry due to 'fast' depolarization, background, multiple lines etc., and t the measuring time of the exponential decay curve. For the positron range the formula used is $R(\text{g/cm}^2) = 0.89 + 0.533\text{E} - 0.0038\text{E}^2$ with E in MeV. For a typical case we can estimate the measuring time $t_{10\%}$ for $n = 10^3\ \text{g}^{-1}\ \text{s}^{-1}$, $m = 10$ g, $(\Omega/4\pi) = 0.1$, $r = 0.06$, $T2 = 0.2\ \tau_\mu$, $t = \tau_\mu$, $T = 4\ \text{g/cm}^2$. From Fig. 39 one finds the 'ideal' absorber to be $D = 12\ \text{g/cm}^2$ ($F(T, D) = 1160$). These values require a measuring time of $t_{10\%} = 32$ min.

Appendix B

In this Appendix the evaluation of the dipolar field tensors introduced in Section III is discussed and results for various lattice structures and muon sites are presented.

Let us first consider a magnetic structure where the direction of the localized magnetic moments varies periodically in space:

$$\mu_j(\vec{m}) = \mu_j \cos(\vec{p} \cdot \vec{m} + \phi). \tag{B1}$$

Then, the sum

$$B_{\text{dip},i}(\vec{R}_\mu) = \sum_{\vec{m}} D_{ij}(\vec{m} - \vec{R}_\mu)\mu_j(\vec{m}) \tag{B2}$$

over an infinite lattice is convergent and the dipolar field at the muon may be obtained by extending the sum over the lattice points of the sample to a sum over an infinite lattice, provided that the period $\vec{p}$ satifies $|\vec{p}|\, L \gg 1$ where L is a typical dimension of the magnetic domain where (B1) applies. Since the direction of $\vec{B}_{\text{dip}}$ in (B2) varies from one unit cell to the next it is preferable to calculate the real and imaginary parts of the lattice periodic quantity

$$B_{\text{dip},i}(\vec{R}_\mu) \exp(-i\vec{p} \cdot R_\mu) = E_{ij}(\vec{R}_\mu; \vec{p})\mu_j, \tag{B3}$$

where the dipolar tensor E is given by

$$E_{ij}(\vec{r}; \vec{p}) = \sum_{\vec{m}} D_{ij}(\vec{m} - \vec{r}) \exp[i\vec{p} \cdot (\vec{m} - \vec{r})]. \tag{B4}$$

For helical structures, this sum converges slowly and an Ewald method is required to achieve rapid numerical convergence. The procedure has been discussed in Ref. 7 and only the results will be summarized here. Splitting the sum into a summation over the direct and one over the reciprocal lattice:

$$E_{ij}(\vec{r}; \vec{p}) = E_{ij}^{\text{dir}}(\vec{r}; \vec{p}) + E_{ij}^{\text{rec}}(\vec{r}; \vec{p}) \tag{B5}$$

one has

$$E_{ij}^{\text{dir}}(\vec{r}; \vec{p}) = \sum_{\vec{m}} F_{ij}(\vec{m} - \vec{r}) \exp[i\vec{p} \cdot (\vec{m} - \vec{r})]. \tag{B6}$$

with

$$F_{ij}(\vec{x}) = D_{ij}(\vec{x})[\text{erfc}(Gx) + \pi^{-1/2}(2Gx + \tfrac{4}{3}G^3x^3) \exp(-G^2x^2)], \tag{B7}$$

where D_{ij} is given by

$$D_{ij}(\vec{x}) = (3x_i x_j - \delta_{ij} x^2)/x^5 \tag{B8}$$

and where erfc denotes the complementary error function. The sum over reciprocal lattice vectors $\vec{g}$ is

$$E_{ij}^{\text{rec}}(\vec{r};\vec{p}) = \frac{N}{V}\sum_{\vec{g}} \tilde{D}_{ij}(\vec{g}-\vec{p}) \exp\left[-i\vec{g}\cdot\vec{r} - (\vec{g}-\vec{p}^2/4G^2\right] \tag{B9}$$

with

$$\tilde{D}_{ij}(\vec{k}) = -\frac{4\pi}{k^2}(k_i k_j - \tfrac{1}{3}\delta_{ij}k^2). \tag{B10}$$

By an appropriate choice of the arbitrary parameter G rapid convergence of each of the sums (B6) and (B9) can be achieved.

In Fig. 40 we plot the calculated dipolar tensor component E_{xx} for a hcp structure for both the tetrahedral and octahedral interstitial sites and the substitutional site as a function of the turn angle of the magnetization from one layer to the next. This particular case applies to the helical structure of Dy in the temperature region $85\,\text{K} < T < 178\,\text{K}$ where the vector $\vec{p}$ introduced in (B1) points along the hexagonal (z) axis. For zero angle E_{xx} is given by

$$E_{xx}(p=0) = \frac{4\pi}{3}\frac{N}{V} + E'_{xx}, \tag{B11}$$

where $N/V = 4/(\sqrt{3}\,ca^2)$ for an hcp lattice and where $E'_{xx} = -E'_{zz}/2$ is given by (B14).

As discussed in Section III, for a ferromagnetic alignment of the localized moments, the dipolar sum over an infinite lattice is only conditionally convergent. One can treat the shape-dependent parts separately, being left with a summation

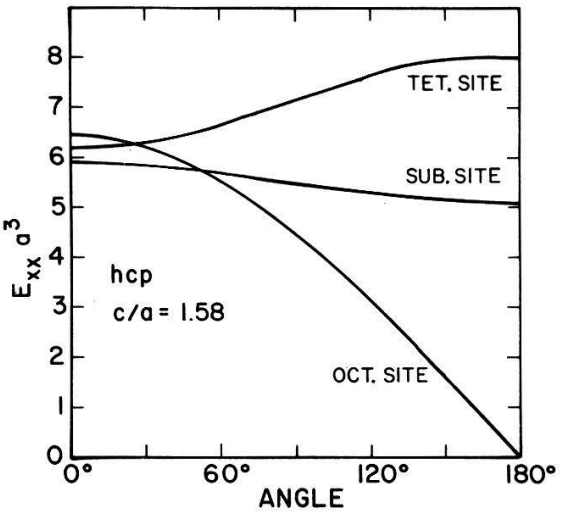

Fig. 40
Dipolar field tensor E_{xx} for the tetrahedral and octahedral interstitial sites and the substitutional site in the helical structure of hcp Dy.

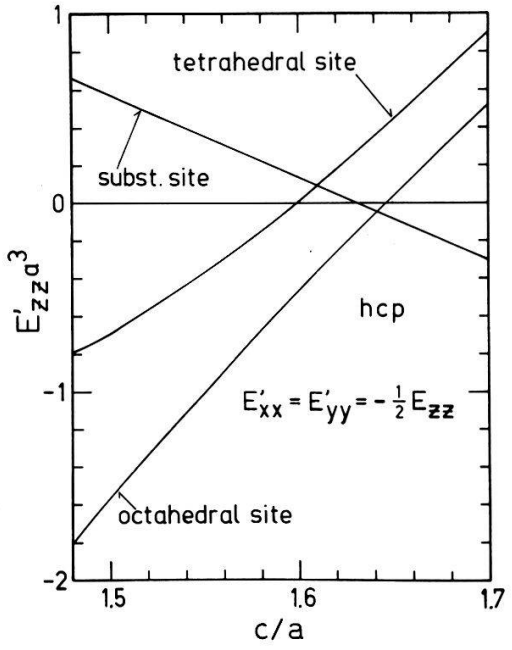

Figure 41
Dipolar field tensor components E'_{zz} plotted as a function of the c/a ratio for the tetrahedral and octahedral interstitial sites and the substitutional site in the hcp lattice.

over the dipole moments within the Lorentz volume Ω which is chosen here to be a sphere. Then, the residual dipolar field tensor is given by

$$E'_{ij}(\vec{r}) = \sum_{\vec{m}} F_{ij}(\vec{m} - \vec{r}) + \frac{N}{V} \sum_{\vec{g} \neq 0} \tilde{D}_{ij}(\vec{g}) \exp[-i\vec{g} \cdot \vec{r} - g^2/4G^2], \tag{B12}$$

where F and $\tilde{D}$ are given by (B7) and (B10). This formula applies for interstitial sites $\vec{r} \neq \vec{m}$. The formula for a substitutional site reads

$$E'_{ij}(\text{subst}) = \sum_{\vec{m} \neq 0} F_{ij}(\vec{m}) + \frac{N}{V} \sum_{\vec{g} \neq 0} \tilde{D}_{ij}(\vec{g}) \exp(-g^2/4G^2). \tag{B13}$$

For the hcp lattice the dipolar tensors $E'_{zz} = -2E'_{xx} = -2E'_{yy}$ for the tetrahedral, the octahedral, and the substitutional sites are shown in Fig. 41 as a function of the c/a ratio. In the range $1.46 < c/a < 1.72$ E'_{zz} may be approximated within an accuracy of 2×10^{-4} by the following polynomials

$$\begin{aligned}
E'_{zz}(\text{oct}) &= [-18.28886 - 3.45220(c/a) + 22.89155(c/a)^2 \\
&\quad -11.25132(c/a)^3 + 1.65186(c/a)^4]\, a^{-3}, \\
E'_{zz}(\text{tet}) &= [461.04497 - 1063.78637(c/a) + 907.14506(c/a)^2 \\
&\quad -340.76642(c/a)^3 + 47.99015(c/a)^4]\, a^{-3}, \\
E'_{zz}(\text{subst}) &= [-18.89859 + 51.80966(c/a) - 44.87532(c/a)^2 \\
&\quad +15.70153(c/a)^3 - 2.02592(c/a)^4]\, a^{-3}.
\end{aligned} \tag{B14}$$

For the bcc lattice both the octahedral and tetrahedral interstitial site have tetragonal symmetry. Hence there are three inequivalent octahedral (tetrahedral)

interstitial sites with non-vanishing components of E' given by

$$\text{oct. site: } E'_{33} = -2E'_{11} = -2E'_{22} = 21.414/a^3$$
$$\text{tetr. site: } E'_{33} = -2E'_{11} = -2E'_{22} = -6.073/a^3,$$

where a is the cubic lattice constant.

As an example Gd(hcp) and Fe(bcc) are considered (see Figs. 15, 23). For Gd one gets at 0 K with the parameters $a = 3.628$ Å, $c/a = 1.5973$, $\mu = 7.55\ \mu_B^e$, and for $\theta = 30°$ (angle between the c-axis and the magnetic Gd-moments)

$$\begin{aligned} B'_{\text{dip}}(\text{oct}) &= (0.277, 0, -0.961) \times 658\ \text{G} \\ B'_{\text{dip}}(\text{tet}) &= (0.277, 0, -0.961) \times 20\ \text{G} \\ B'_{\text{dip}}(\text{sub}) &= (0.277, 0, -0.961) \times 217\ \text{G} \end{aligned} \tag{B16}$$

For Fe one gets at 0 K ($a = 2.872$ Å, $\mu = 2.21\ \mu_B^e$) for a magnetization along [001], for the sites with the tetragonal axis along [001]

$$\begin{aligned} B'_{\text{dip}}(\text{oct}) &= +18.52\ \text{kG} \\ B'_{\text{dip}}(\text{tet}) &= -5.25\ \text{kG}, \end{aligned} \tag{B17}$$

and for the sites with the tetragonal axis along [100] and [010]

$$\begin{aligned} B'_{\text{dip}}(\text{oct}) &= -9.26\ \text{kG} \\ B'_{\text{dip}}(\text{tet}) &= +2.63\ \text{kG}. \end{aligned} \tag{B18}$$

For Fe magnetized along [111] the dipolar fields at the two sites are perpendicular to the direction of magnetization with magnitudes:

$$\begin{aligned} B'_{\text{dip}}(\text{oct}) &= 13.10\ \text{kG} \\ B'_{\text{dip}}(\text{tet}) &= 3.72\ \text{kG}. \end{aligned} \tag{B19}$$

REFERENCES

[1] R. L. Garwin, L. M. Lederman, and M. Weinrich, Phys. Rev. *105*, 1415 (1957).
[2] J. H. Brewer and K. M. Crowe, Ann. Rev. Nucl. Part. Sci. *28*, 239 (1978).
[3] *Proc. First Int. Top. Meeting on Muon Spin Rotation* (Rorschach 1978), edited by F. N. Gygax, W. Kündig, and P. F. Meier (North Holland Publ. Comp., Amsterdam 1979), and Hyperfine Interactions Vol. 6, No 1 (1979).
[4] *IUPAP Report on Symbols, Units, and Nomenclature in Physics*, Physica A *93*, 1 (1978).
[5] T. Kinoshita and A. Sirlin, Phys. Rev. *113*, 1652 (1959).
[6] B. D. Patterson, A. Hintermann, W. Kündig, P. F. Meier, F. Waldner, H. Graf, E. Recknagel, A. Weidinger, and T. Wichert, Phys. Rev. Lett *40*, 1347 (1978).
[7] P. F. Meier, W. Kündig, B. D. Patterson, and K. Rüegg, Hyperfine Interactions *5*, 311, (1978).
[8] H. P. Myers and W. Sucksmith, Proc. Roy. Soc. (London), Ser. A, *207*, 427 (1951).
[9] J. Crangle, Phil. Mag. *46*, 499 (1955).
[10] E. F. Bertaut, A. Delapalme, and R. Pauthenet, Solid State Commun. *1*, 81 (1963).
[11] H. Graf, W. Kündig, B. D. Patterson, W. Reichart, P. Roggwiller, M. Camani, F. N. Gyrax, W. Rüegg, A. Schenck, H. Schilling, and P. F. Meier, Phys. Rev. Lett. *37*, 1644 (1976).
[12] S. Müller, Ph. Dünner, and N. Schmitz-Pranghe, Z. Angew. Phys. *22*, 403 (1967).
[13] I. S. Bolgov, Yu. N. Smirnov, and V. A. Finkel, Phys. Metals Metallog. *17*, No. 5, 76 (1964).
[14] R. M. Moon, Phys. Rev. *A136*, 195 (1964).
[15] F. Menzinger, A. Paoletti, Phys. Rev. Lett. *10*, 290 (1963).

[16] R. J. Weiss, Phys. Rev. Lett. *11*, 264 (1963).
[17] J. Kanamori, in Magnetism I, edited by G. T. Rado, H. Suhl (Academic Press, New York and London (1963)).
[18] R. R. Birss and D. J. Martin, J. Phys. *C8*, 189 (1975).
[19] L. Néel, H. Phys. Radium, Paris, *5*, 241 (1944).
[20] W. Sucksmith, J. E. Thompson, Proc. Roy. Soc. (London), Ser. *A255*, 362 (1954).
[21] R. M. Bozorth, Phys. Rev. *96*, 311 (1954).
[22] J. S. Kouvel, C. C. Hartelius, J. Phys. Chem. Solids *25*, 1357 (1964).
[23] R. Pauthenet, Y. Barnier, and G. Rimet, J. Phys. Soc. Japan *17*, suppl. B1, 309 (1962).
[24] H. E. Nigh, S. Legvold, and F. H. Spedding, Phys. Rev. *132*, 1092 (1963).
[25] R. M. Moon, W. C. Koehler, J. W. Cable, and H. R. Child, Phys. Rev. B5, *997* (1972).
[26] W. D. Corner and B. K. Tanner, J. Phys. C, *9*, 627 (1976).
[27] W. D. Corner, W. C. Roe, and K. N. R. Taylor, Proc. Phys. Soc. (London) *80*, 927 (1962).
[28] J. W. Cable and E. O. Wollan, Phys. Rev. *165*, 733 (1968).
[29] C. D. Graham, J. Phys. Soc. Japan *17*, 1310 (1962).
[30] I. I. Gurevich, A. I. Klimov, V. N. Maĭorov, E. A. Meleshko, B. A. Nikol'skiĭ, A. V. Purogov, V. S. Roganov, V. I. Selivanov, and V. A. Suetin, Zh. Eksp. Teor. Fiz. *69*, 1453 (1975) [Sov. Phys.-JETP *42*, 741 (1976)].
[31] H. Graf, W. Hofmann, W. Kündig, P. F. Meier, B. D. Patterson, and W. Reichart, Solid State Commun. *23*, 653 (1977).
[32] J. R. Banister, S. Legvold, and F. H. Spedding, Phys. Rev. *94*, 1140 (1954).
[33] Y. S. Touloukian, *Thermophysical Properties of Matter*, Volume *12* (IFI/Plenum New York–Washington).
[34] J. J. Rhyne, in: *Magnetic Properties of Rare Earth Metals*, edited by R. J. Elliott (Plenum, London, 1972).
[35] M. K. Wilkinson, W. C. Koehler, E. A. Wollan, and J. W. Cable, J. Appl. Phys. *32*, 48S, (1961).
[36] F. J. Darnell and E. P. Moore, J. Appl. Phys. *34*, 1337 (1963).
[37] F. J. Darnell, Phys. Rev. *130*, 1825 (1963).
[38] W. D. Corner and J. Welford, J. Magnetism and Magn. Mat. *3*, 212 (1976).
[39] P. B. Fynbo, J. Phys. *F7*, 1349 (1977) and private communication.
[40] D. R. Behrendt, S. Legvold, and F. H. Spedding, Phys. Rev. *109*, 1544 (1958).
[41] I. I. Gurevich, A. I. Klimov, V. N. Maiorov, B. A. Nikol'skiĭ, V. S. Roganov, V. I. Selivanov, and V. A. Suetin, Zh. Eksp. Teor. Fiz. *23*, 345 (1976) [JETP Lett. *23*, 310 (1976)].
[42] W. Hofmann, W. Kündig, P. F. Meier, B. D. Patterson, K. Rüegg, O. Echt, H. Graf, E. Recknagel, A. Weidinger, and T. Wichert. Phys. Lett. *A65*, 343 (1978).
[43] G. J. Bowden, D. S. P. Bunbury, and J. M. Williams, Proc. Phys. Soc. *91*, 612 (1967).
[44] J. Crangle and G. M. Goodman, Proc. Roy. Soc. Lond., *321A*, 477 (1971).
[45] M. L. G. Foy, N. Heiman, W. J. Kossler, and C. E. Stronach, Phys. Rev. Lett. *30*, 1064 (1973).
[46] I. I. Gurevich, A. I. Klimov, V. N. Maiorov, E. A. Meleshko, I. A. Muratova, B. A. Nikol'skii, V. S. Roganov, V. I. Selivanov, and V. A. Suetin, Zh. Eksp. Teor. Fiz. *66*, 374 (1974) [Sov. Phys. JETP *39*, 178 (1974)].
[47] H. Graf, W. Kündig, B. D. Patterson, W. Reichart, P. Roggwiller, M. Camani, F. N. Gygax, W. Rüegg, A. Schenck, and H. Schilling, Helv. Phys. Acta, *49*, 730 (1976).
[48] N. Nishida, R. S. Hayano, K. Nagamine, T. Yamazaki, J. H. Brewer, D. M. Garner, D. G. Fleming, T. Takeuchi, and Y. Ishikawa, Solid State Commun. *22*, 235 (1977).
[49] H. Graf, E. Holzschuh, E. Recknagel, A. Weidinger, T. Wichert, Hyperfine Interactions *6*, 245 (1979).
[50] R. I. Grynszpan, N. Nishida, K. Nagamine, R. S. Hayano, T. Yamazaki, J. H. Brewer, and D. G. Fleming, Solid State Commun. *29*, 143 (1979).
[51] I. I. Gurevich, A. N. Klimov, V. N. Maiorov, E. A. Meleshko, B. A. Nikol'skii, V. S. Roganov, V. I. Selivanov, V. A. Suetin, ZhETF Pis. Red. *18*, 564 (1973) (JETP Lett. *18*, 332 (1973)).
[52] B. D. Patterson, K. M. Crowe, F. N. Gygax, R. F. Johnson, A. M. Portis, J. H. Brewer, Phys. Lett. *A46*, 453 (1974).
[53] K. Nagamine, S. Nagamiya, O. Hashimoto, N. Nishida, T. Yamazaki, and B. D. Patterson, Hyperfine Interactions *1*, 517 (1976).
[54] H. Graf, E. Holzschuh E. Recknagel, A. Weidinger, and T. Wichert, Hyperfine Interactions *6*, 245 (1979).

[55] O. ECHT, H. GRAF, E. HOLZSCHUH, E. RECKNAGEL, A. WEIDINGER, T. WICHERT, Hyperfine Interactions *6*, 329 (1979).
[56] A. ABRAGAM, *Principles of Nuclear Magnetism*, Chapt. X (Clarendon Press, Oxford 1961).
[57] E. DANIEL and J. FRIEDEL, J. Phys. Chem. Solids *24*, 1601 (1963).
[58] C. G. SHULL and H. A. MOOK, Phys. Rev. Lett. *16*, 184 (1966).
[59] H. A. MOOK and C. G. SHULL, J. Appl. Phys. *37*, 1034 (1966).
[60] C. G. SHULL, in *Magnetic and Inelastic Scattering of Neutrons by Metals*, Eds. T. J. ROWLAND and P. A. BECK, (Gordon and Breach, New York 1967).
[61] These values correspond to $B_0 = 4\pi M_0 = 1.0 \pm 0.8$ kG and -1.6 ± 0.5 kG which were reported in Ref. 60 and differ from the values mentioned in the older work (Ref. 58).
[62] K. G. PETZINGER and R. MUNJAL, Phys. Rev. *B15*, 1560 (1977).
[63] B. D. PATTERSON and J. KELLER, Hyperfine Interactions *6*, 73 (1979).
[64] H. KATAYAMA, K. TERAKURA, and J. KANAMORI, Solid State Commun. *29*, 431 (1979).
[65] B. N. HARMON and A. J. FREEMAN, Phys. Rev. *B10*, 1979 (1974).
[66] A. BLANDIN and I. A. CAMPBELL, Phys. Rev. Lett. *31*, 51 (1973).
[67] P. F. MEIER, Solid State Commun. *27*, 1163 (1978).
[68] P. F. MEIER, W. KÜNDIG, and K. RÜEGG, Hyperfine Interactions *6*, 77 (1979).
[69] P. JENA, Hyperfine Interactions *6*, 5 (1979) and references cited therein.
[70] P. RAGHAVAN, M. SENBA, and R. S. RAGHAVAN, Phys. Rev. Lett. *39*, 1547 (1977).
[71] P. F. MEIER and A. B. DENISON, J. Appl. Phys. (in press).